Commissioning of a FADC-based data acquisition system for the KASCADE-Grande experiment

DIPLOMARBEIT
zur Erlangung des akademischen Grades
Diplom-Physiker

dem Fachbereich Physik der
Universität Siegen

vorgelegt von
Thomas Bäcker

August 2005

Contents

Chapter 1

Introduction

1.1 Astroparticle physics

At the end of the 19th century, Becquerel discovered that radioactive sources were emitting ionizing particles; the ionizing effect of those particles was held responsible for the charge leakage observed with electroscopes in the presence of a radioactive source. However, it was found that even in absence of such a source, the accumulated charge would start reducing slowly. In order to find out whether the leakage was caused by environmental radioactivity, probably mainly emitted by the earth's surface, Thomas Wulf measured the amount of charge leakage vs. the altitude above sea level. He found, that the loss of charge was indeed reduced noticeably depending on the altitude reached. The measurements were performed on top of buildings or small mountains only, therefore Wulf did not reach altitudes beyond 500 m.

As a consequence, Victor Hess started to undertake similar measurements at even higher altitude by using a balloon to be able to ascend arbitrarily high. He could thereby confirm, that the ionizing radiation was indeed diminishing while the distance to the earth's surface was increasing. At about 1500 m, however, Hess observed that the intensity of ionizing radiation was increasing again. He found that the radiation became even more intense while the balloon ascended further; this led to the conclusion that there was probably a source of radiation in the highest layers of the atmosphere or even beyond, that made ionizing particles come in from above.

About one decade later, again balloons were used to further examine the properties of the radiation, which had already been detected by Hess. This time, Robert Millikan discovered, that the radiation coming in from above causes changes of the composition of the atmosphere, i.e. the collision of incoming primary particles with atmospheric constituents converts the latter into secondary particles. The entity of those primary particles is usually referred to as "cosmic rays". About 85% of the primary particles are protons, 12% are α-particles, only about 2% are electrons. The remaining fraction consists mainly of heavier components, i.e. nuclei of heavy elements, although photons and neutrinos have been detected as well. Antiparticles are, however, very rarely found in cosmic rays; the probability of detecting an antiproton is only 10^{-4} compared to that of detecting a proton.

Already a few years after the cosmic rays and secondary particles rays had been explored by Millikan, individual particles could be identified, e.g. the pion, the muon, the kaon and the positron by using photographic plates and cloud chambers [6].

In the late 1930s, while Pierre Auger was conducting experiments on cosmic rays, he observed that many particle detections occurred in several detectors coincident in time, although the detector stations had been placed far apart. Auger concluded, that the coincident particle incidences were caused by particle cascades originating from interactions of cosmic ray primaries with atmospheric particles. From the measurements of those particle cascades—usually referred to as *extensive air showers*—it became possible to determine an upper limit for the energy of cosmic ray particles; according to this estimate, the energy was ranging up to 1 PeV. Nowadays, experiments like KASCADE-Grande are capable of detecting particles resulting from primaries carrying up to some EeV of energy. In 1994, the Fly's Eye experiment even reported the detection of a 320 EeV cosmic ray [30] event.

The energy spectrum of cosmic rays is usually described as the particle flux I as a function of energy E divided by the energy interval dE. The energy spectrum can approximately be expressed by a power law for several orders of magnitude:

$$\frac{dI}{dE} \propto E^{-\lambda}, \tag{1.1}$$

where λ is called the spectral index.

The value of λ equals 2.7 for energies exceeding 100 GeV and ranging up to 3 PeV, where the spectrum is slightly bent downwards; this kink is called the "knee". Beyond this energy, the spectral index rises to 3.1; at about 300 PeV, another dip of the spectrum will presumably be observed, often referred to as the "second knee". At the "ankle" of the spectrum—at an energy of 3 EeV—the spectral index returns to a value of 2.7; the spectrum is therefore bent upwards at this point [5]. For energies exceeding 60 EeV, a cut-off has been predicted by Greisen, Zatsepin and Kuz'min; it is caused by interactions of the primaries with microwave background photons [5]. See figure 1.1 for results from experimental data.

Recent results of the KASCADE experiment indicate that the "knee" is caused by the decrease of the flux of light particles, whereas heavier components do not exhibit such a drop up to energies of at least 10 PeV [10].

Currently, there are several theoretical attempts trying to explain the kinks of the spectrum:

- the acceleration mechanism could be the reason for the change of the spectral index [5] in the knee energy range; the maximum energy, that can be reached during acceleration, equals the knee energy and is proportional to the charge of the respective particle and the size of the space region, where the acceleration takes place. Furthermore, it depends on the magnetic field strength within that region. The energy limit would therefore differ for nuclei, which are very different in terms of charge, but originate from the same space region;

- another approach considers the diffusion due to high-energy particles escaping from the galaxy to be responsible for the spectral kinks [11]. The magnetic field strength within the space region could suffice to restrict particles to that region up to a maximum energy, which equals the knee energy and is proportional to the charge of the primary. Particles carrying higher energies would be able to escape from the space region. Thus, at this energy threshold, there would be a sudden change in the number of particles, that contribute to cosmic rays, eventually resulting in a kink at the knee energy in the measured spectrum;

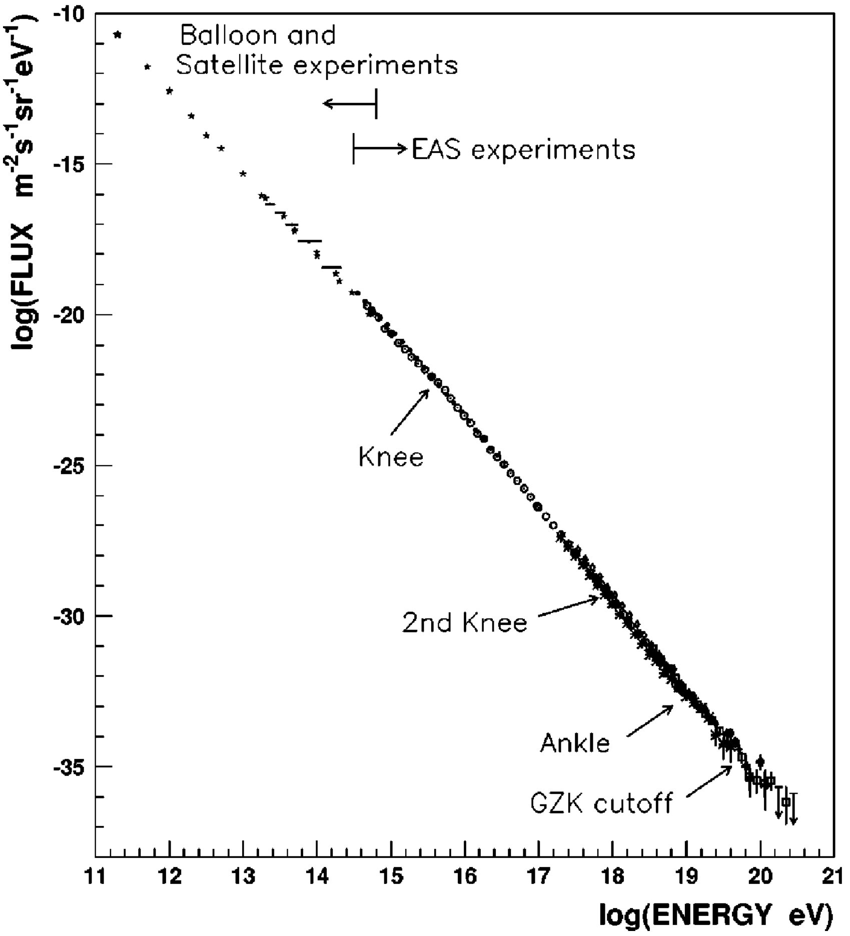

Figure 1.1: Energy spectrum of primary cosmic rays in differential form. Spectral data below 1 PeV is measured using direct detection of cosmic ray particles, whereas the spectrum above that energy is obtained using EAS experiments [12]. The GZK cut-off is caused by interactions of cosmic rays with microwave background photons.

- the energy of primary particles could partially be diverted into hadronic interaction channels, either in the atmosphere or in the interstellar matter. Beyond a threshold energy, which coincides with the knee energy, these hadronic interaction channels open up. Since these interaction channels are currently not taken into account for the reconstruction of primary energies, this would actually result in lower reconstructed contributions to the high energy region of the spectrum [10]. In this case, the knee energy should depend on the mass of the primary instead of its charge.

Direct means of measuring cosmic rays, e.g. via satellite experiments, offer only a limited detection area. Since the particle flux for energies above 1 PeV would be too low to achieve sufficient statistics using this direct type of detection method, only experiments situated on earth allow the measurement of particles in the PeV or even EeV range. Ground based experiments use the earth's atmosphere both as a target and as a calorimeter. The detection area of experiments located on ground can be expanded to comply with the requirements and there is no obvious limit with respect to the operating duration. The drawback involved in building a ground based experiment for cosmic ray detection is, however, that the primary particles cannot be measured directly, since they do not pass through the detectors but collide with atmospheric constituents beforehand. The particles detected by the detector setup on the ground are, in fact, the secondary particles produced during those collisions as well as particles produced as a result of cascades of interactions of the secondary particles with atmospheric components. The main properties of those "extensive air showers" are described in the following section.

1.2 Extensive air showers (EAS)

Whenever a particle cascade is initiated by a primary cosmic ray particle, it depends—among other things—on the total primary energy and the altitude of the first interaction, whether any secondary particle will reach the ground or not and if so, how many of them will get through to the earth's surface. Since the primary energy is diverted into several ramifications of the cascade, while the secondaries are undergoing particle interactions and are propagating in space, the total number of particles is directly correlated to the primary's energy. Thus, the primary energy feed can be estimated from the particle densities detected on ground, while the chemical composition of the cosmic rays can be derived from the ratio of the encountered muons and electrons. The incidence direction of particular cosmic rays can be calculated from the arrival times of air shower constituents.

Air showers originating from primaries of energies below several TeV do not contribute to particle incidences on ground level in a noticeable way, since the cascade will already have dissipated all kinetic energy on higher altitude levels. However, when fed with primary energies of at least some PeV, an air shower can result in millions of secondaries on sea level. A schematic view of a particle shower's spatial development is shown in figure 1.2(b). Here, the *shower axis* is determined by the trajectory of the cosmic ray particle extrapolated beyond the place of the primary interaction. The slightly curved area shown is called the *shower front*, which is formed by the shower particles travelling through the atmosphere with nearly the vacuum speed of light. Its thickness depends on the distance from the shower axis. The plane, which is tangent to the shower front and perpendicular to the shower axis, is usually referred to as the *shower plane* [15].

Several processes take place during the development of an extensive air shower, e.g. particles are produced, decay, lose energy due to ionization of atmospheric matter, are subject to elastic scattering.

An extensive air shower consists mainly of three constituents: the hadronic, the muonic and the electromagnetic component; see figure 1.2(a) for an illustration.

Pions and kaons as well as baryons constitute the hadronic component of an air shower. During interactions these particles receive most of their momenta in forward direction, i.e. they end up moving in parallel to and near the shower axis which is determined by the direction of the particular cosmic ray particle; that is, they are moving inside a thin cone around that axis. Most of the hadrons produced are neutral pions and they decay after a short life time ($\tau_{\pi^0} \approx 8 \cdot 10^{-17}$s [13]) thereby usually not experiencing any interaction with atmospheric nuclei:

$$\pi^0 \longrightarrow 2\gamma,$$
$$\pi^0 \longrightarrow e^+ + e^- + \gamma.$$

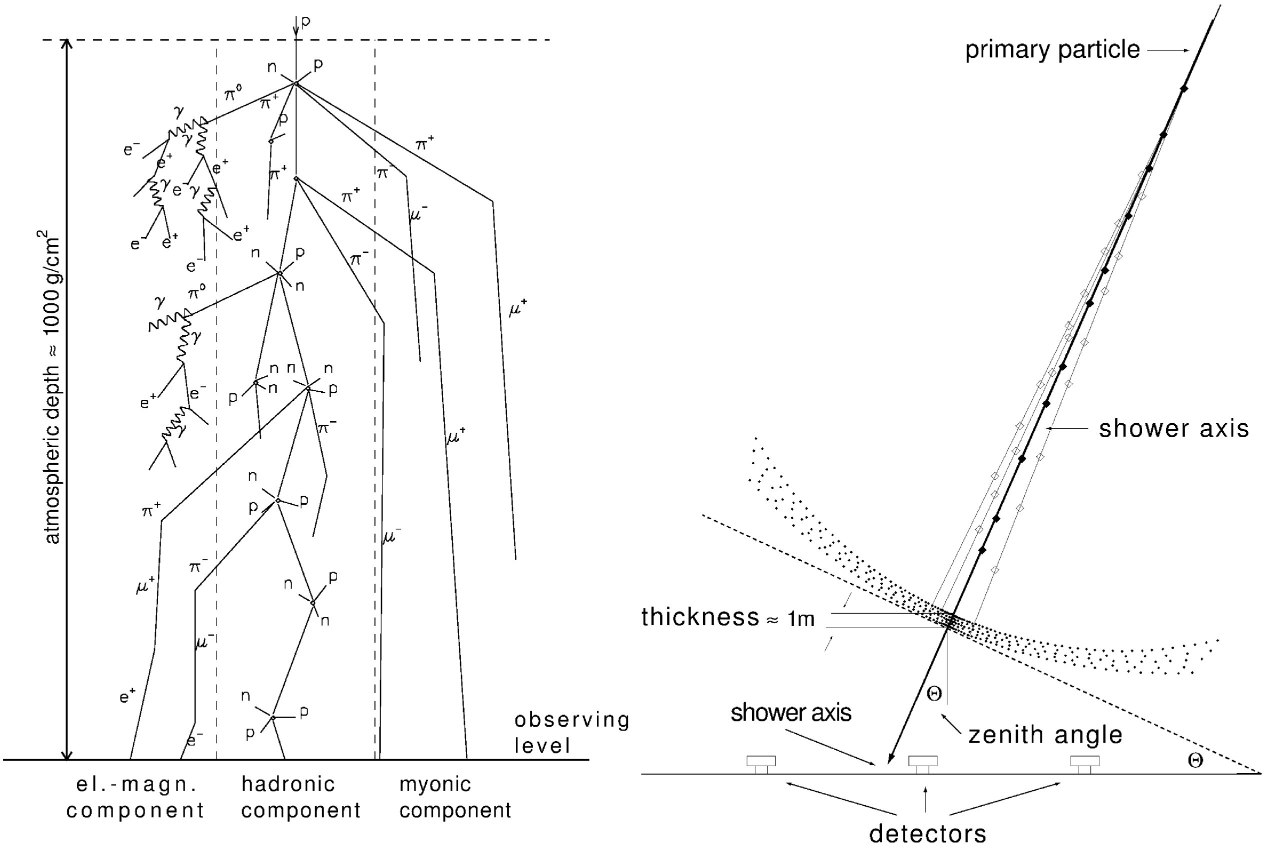

(a) (b)

Figure 1.2: Schematic views of an extensive air shower (EAS) as it is evolving in the atmosphere. In (a) the particle cascades initiated by a primary cosmic ray particle are illustrated while (b) visualizes the spatial structure of an air shower [14].

Here, the latter decay mode only contributes about 1.2%. Both modes feed the electromagnetic shower component by alternating pair production and bremsstrahlung processes until the energy decrease of the secondaries is suppressing the production of electromagnetic constituents in favour of atmospheric ionization. The hadronic shower component is continuously creating neutral pions; therefore, many electromagnetic subshowers are initiated along the way of the hadronic constituents.

Charged pions decay on average after $\tau_{\pi^\pm} \approx 2.6 \cdot 10^{-8}\mathrm{s} \gg \tau_{\pi^0}$ [13]. That is, the probability for interactions is significantly higher than for the neutral pions due to the longer mean path length until they decay. Thus, the charged pions create additional hadrons which then will contribute to the hadronic shower component again.

The decaying $\pi^\pm$ pions create the muonic component of the air shower according to

$$\pi^+ \longrightarrow \mu^+ + \nu_\mu,$$
$$\pi^- \longrightarrow \mu^- + \overline{\nu}_\mu.$$

Another share of the muons is originating from kaon decays:

$$K^+ \longrightarrow \mu^+ + \nu_\mu,$$
$$K^- \longrightarrow \mu^- + \overline{\nu}_\mu.$$

The probability for low energy muons to arrive on sea level is rather low; they usually decay beforehand due to their short life time of $\tau_\mu \approx 2.2 \cdot 10^{-6}$s [13], whereas high energy muons do not decay along their way downwards, since they are subject to relativistic time dilatation due to the amount of kinetic energy they are carrying. Approximately 100% of the muons decaying initiate electromagnetic subshowers via [13]:

$$\mu^+ \longrightarrow e^+ + \nu_e + \overline{\nu}_\mu,$$
$$\mu^- \longrightarrow e^- + \overline{\nu}_e + \nu_\mu.$$

Since the muonic component does not undergo strong interactions, its energy loss is barely caused by ionization processes because of the muon mass, which is large compared to that of e.g. an electron and consequently suppresses the emission of bremsstrahlung [6].

Neither the muonic nor the electromagnetic component of an air shower must necessarily have been initiated as a subshower; with a negligible probability the primary cosmic ray particle may have been a muon or a photon already—see section 1.1.

1.3 Scope of this thesis

This thesis deals with the commissioning of a high performance FADC-based data acquisition system which has been developed and built at the University of Siegen and is now operated in the Grande array in parallel to the original Grande DAQ system since July 2005. The measures that were taken in order to achieve proper concurrent operation of both data acquisition systems are described, thereby suggesting the following sectioning:

- Chapter 2 contains a description of the KASCADE-Grande experiment, its aims and the setup of its detectors;
- In chapter 3, the components of the original Grande setup, which are relevant with respect to the concurrent operation of the FADC-based DAQ system, are discussed and analyzed in depth;
- An overview of the FADC-based DAQ system is presented in chapter 4;

- Methods, which have been considered to operate the DAQ systems in parallel, are discussed in chapter 5;
- Technical properties of the KGEMD component of the FADC-based DAQ system are discussed in chapter 6;
- In chapter 7, a summary of the contents is presented.

Chapter 2

The EAS experiment KASCADE-Grande

The KASCADE-Grande experiment is a ground-based detector setup used for the exploration of extensive air showers (EAS) initiated by primaries, which are carrying energies from several 100 TeV up to some EeV. Since 1996, it is operated on the site of the Forschungszentrum Karlsruhe in southern Germany, at about 110 m above sea level. In order to achieve sufficient statistics in the PeV range, a large area sensitive to all kinds of shower particles is mandatory; in addition, the duration of the experiment has to be chosen accordingly, so enough data sets of particles carrying PeV energies can be collected. The KASCADE setup was built with these design goals in mind. Several years after the KASCADE setup had been commissioned, the Grande array was added in order to increase the sensitive detection area of the experiment, thereby extending the measurable energy up to the EeV range; this is an indispensable prerequisite for the investigation of the "iron knee" region of the spectrum regarding the chemical composition of cosmic rays. Prior to extending the measurable energy range, it would not even have been possible at all to decide whether there is a second knee region and if so, whether it is caused by a decrease of the flux of heavy shower components like iron. The energy range detectable by KASCADE alone and the effect of the Grande extension is shown in figure 2.1(b).

An additional detector array, named *Piccolo*, provides both the KASCADE array and its Grande extension with an event trigger. Thus, the KASCADE-Grande experiment is actually the original KASCADE experiment with the Grande detectors and the Piccolo trigger array added to it; see figure 2.1(a) for an overview of the components. The internal structure of the detector components is described in the following sections; the properties of the particular integral parts are listed in table 2.1.

2.1 The KASCADE component

This component, which was built as a stand-alone experiment in the beginning, consists of several detector units; see figure 2.2.

- An array of 252 scintillator detector stations, located on an area of $200\times200\,\mathrm{m}^2$; this array is capable of measuring arrival times and particle densities of the electromagnetic and muonic shower constituents. The stations are arranged in a regular fashion, with a distance of 13 m between them. Clusters of 16 stations are combined with respect to the trigger logic of the KASCADE data acquisition system. The inner four clusters are lacking one station each due to the fact, that the central detector is occupying the space; these clusters are not equipped with dedicated muon detectors either. In contrast, the separation of muons from the electromagnetic shower component is enabled in the surrounding 12 clusters through the use of e/γ attenuating lead/iron layers placed right between the scintillators for e/γ and μ particles, respectively. Whenever a coincident energy deposit is encountered by at least five stations of a cluster, a trigger signal is generated, serving as the main KASCADE trigger; the trigger condition corresponds to a threshold of some 100 TeV [16].

- The *central detector*, enclosed by the innermost four array clusters; a schematic view of its internal structure is shown in figure 2.3. The central detector aims at investigating the incidence directions and energies of hadrons, especially unaccompanied hadrons, i.e. single hadrons, which are detected at zenith angles below 30 ° and are carrying energies of at least 50 GeV [9]. This detector is comprised as follows (starting with the upmost layer).
  - The *top cluster* fulfills two tasks. First, it compensates for the missing four array stations of the inner clusters by sensing the electromagnetic shower component. Second, it provides trigger signals for small showers. The top cluster consists of 25 scintillation counters covering 1/13 of the total layer.
  - Nine layers of warm liquid ionization chambers, separated by iron absorbers, form the *hadron sampling calorimeter*. The thickness of the absorber layers is increasing from the top to the bottom of the setup in order to distinguish between hadrons of different energy ranges. On top of the first layer, a lead absorber prevents electromagnetic shower components from entering the actual hadron calorimeter. Below the ninth ionization chamber, an additional thick layer of concrete ensures the absorption of hadrons which passed through all upper layers. The nine detection layers contain a total of 10,000 warm liquid ionization chambers, corresponding to a total of 40,000 readout channels to be processed by the KASCADE DAQ system.
  - The *trigger layer* is located below the third absorption layer of the hadron sampling calorimeter. A total of 456 scintillator cells constitute this component, which is used both for the triggering of hadron or muon events and for the determination of arrival times.
  - Muons at energies exceeding 2.4 GeV are detected by a set of *multi-wire proportional chambers* (MWPC) right at the bottom of the central detector, combined with a layer of *limited streamer tubes* (LST) below it.
- North of the central detector, the *muon tracking detector* (MTD) is situated; the major goal of this part of the detector setup is the determination of muon production heights by applying triangulation techniques. The MTD's position as well as a rough side view of its structure is given in figure 2.2. Muons with energies below 0.8 GeV and electromagnetic shower constituents are absorbed by the soil, iron and concrete shielding above the MTD. Muons passing through the shielding are

Detector component	**Total area** $[\mathbf{m^2}]$	**Threshold** [MeV]	**Type of particle**
KASCADE:			
array, liquid scintillators	490	5	e/γ
array, plastic scintillators	622	230	μ
muon tracking detector (MTD), streamer tubes	4 layers ×128	800	μ
central detector:			
calorimeter, liquid ionization chambers	8 layers ×304	$5 \cdot 10^4$	hadrons
trigger layer, plastic scintillators	208	490	μ
top cluster, plastic scintillators	23	5	e/γ
top layer, liquid ionization chambers	304	5	e/γ
multi-wire proportional chambers (MWPC)	2 layers ×129	$2.4 \cdot 10^3$	μ
limited streamer tubes (LST)	250	$2.4 \cdot 10^3$	μ
Grande array	370	3	e/μ
Piccolo array	80	5	e/μ

Table 2.1: Properties of the KASCADE-Grande detector components. For each component, the type of particles to be detected, the total sensitive areas and thresholds for vertically incoming particles are listed [16].

detected by three layers of horizontally aligned limited streamer tubes, which offer an angular resolution of 0.35 ° for vertically incoming muons. Inclined particle tracks are measured by two additional layers of vertically aligned limited streamer tubes [7].

2.2 The Grande extension

In the year 2000, after about ten years of operation, the 37 scintillator detector stations, which had been operated at Campo Imperatore, Gran Sasso National Laboratories in Italy at an altitude of 2005 m above sea level, forming the EAS-TOP experiment [17], were dismantled. They were moved to the Forschungszentrum Karlsruhe, Germany, in order to be reused as the *Grande array*. These detector stations cover an area of $700 \times 700\,\mathrm{m}^2$ on the site. The particular stations are equipped with 16 plastic scintillator cells, arranged in a 4×4 configuration, offering a total sensitive area of $10\,\mathrm{m}^2$ each. A pyramidal optical guide is mounted from below, thereby coupling the scintillation light emitted due to energy deposits inside the scintillator into attached photomultiplier tubes. Each scintillator cell is monitored by a PMT operated in high gain mode, resulting in a dynamic range of 0.3 up to 750 in units of the minimum ionizing particle energy of 10.3 MeV (on average for the angular distribution, corresponding to ≈8.2 MeV for perpendicular particle incidence) [18]. An additional low gain photomultiplier tube is attached to each of the innermost four optical guides; thus, the dynamic range is extended, covering an interval from 0.3 up to 30000 m.i.p. units for the corresponding scintillator cells. The gain setting is accomplished by adjusting the supply voltage of these tubes accordingly. The use of

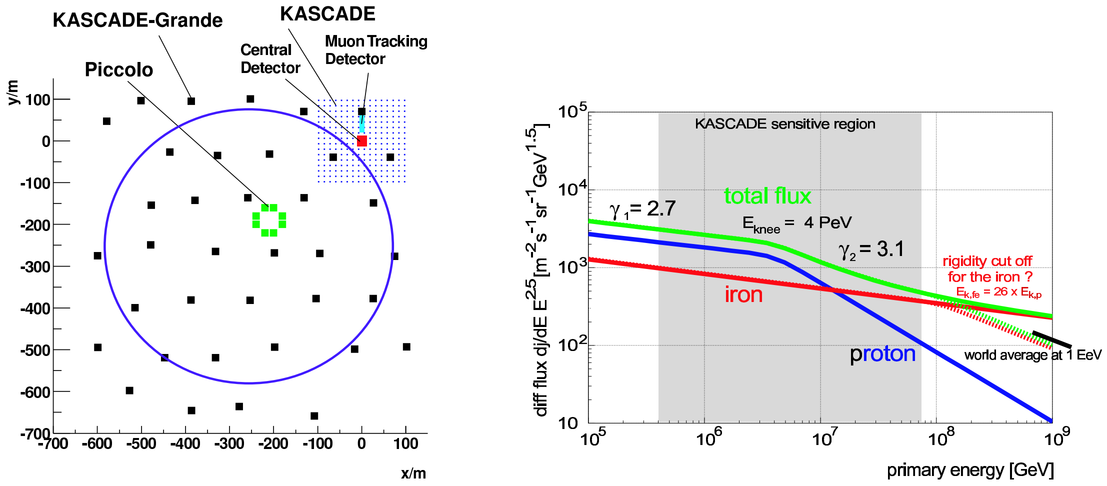

(a) (b)

Figure 2.1: (a) Sketch of the KASCADE-Grande configuration [8]. (b) Energy range covered by KASCADE (grey area) and by incorporating the Grande array (area to the right) [8].

low gain PMTs permits measurements even at high particle densities, where the high gain photomultiplier tubes are saturated.

From the point of view of the original Grande DAQ system, the stations of the Grande extension are arranged in 18 overlapping hexagonal trigger clusters. Besides an external trigger issued by e.g. the Piccolo array or the trigger layer of the central detector, shower data is also acquired whenever either all seven stations of a particular trigger cluster are detecting a particle (named *7/7 coincidence*) or the central station of a particular cluster as well as three of its neighbours are registering a coincident energy deposit (called *4/7 coincidence*). Trigger conditions are hard-wired as an integral part of this DAQ system; therefore, changing the triggering scheme on the fly is not feasible.

An additional FADC-based DAQ system, which has been installed in the Grande array in July 2005, is offering a more flexible triggering scheme; here, trigger conditions are evaluated by means of software, thereby nearly any kind of geometrical or time-like trigger condition may be implemented.

2.3 The Piccolo trigger array

A total of eight detector stations form the octagonal Piccolo trigger array, which is located right between the centres of the KASCADE and Grande arrays. The Piccolo stations contain 10 m^2 plates of scintillating matter, subdivided into 12 cells. Trigger signals are sent to both the Grande and the KASCADE DAQ systems, enabling the systems to perform joint data taking regarding the same air shower event.

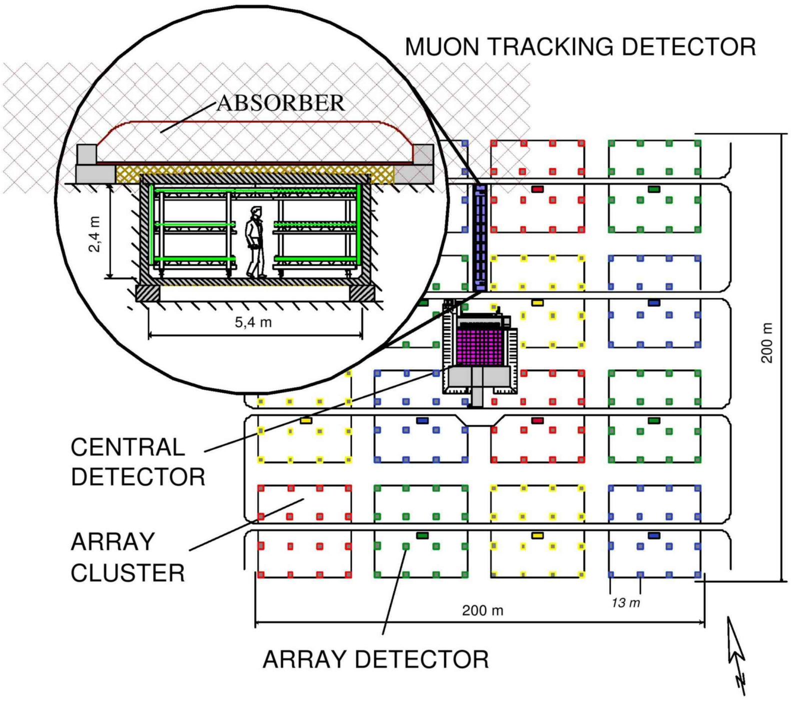

Figure 2.2: Layout of the former KASCADE experiment, which KASCADE-Grande is based upon [7].

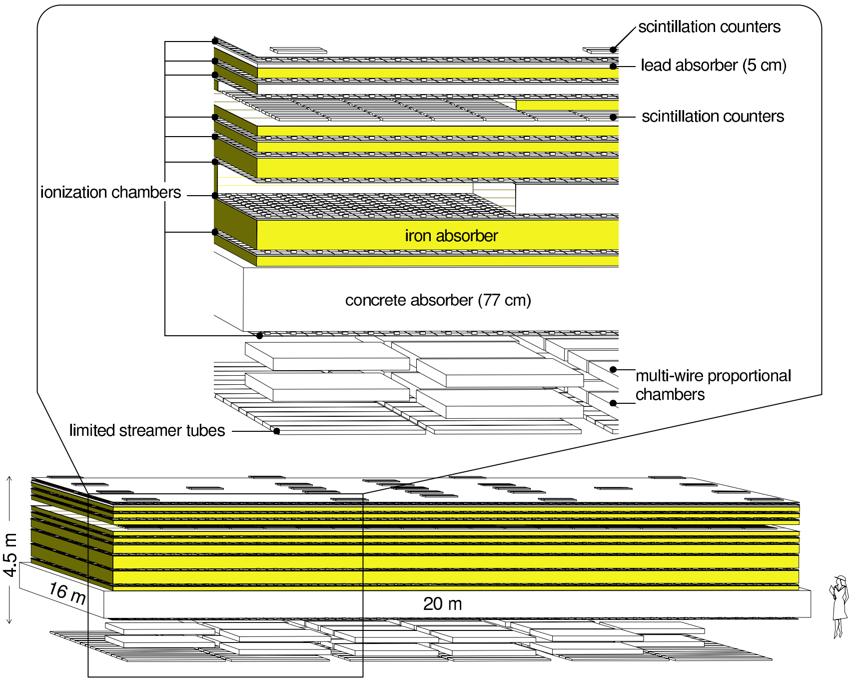

Figure 2.3: Components of the KASCADE central detector [16].

Chapter 3

Components of the original Grande station setup

The FADC-based data acquisition system for the Grande array of the KASCADE-Grande experiment was not intended to run exclusively; i.e. the original Grande DAQ system was not planned to be replaced by the new FADC-based system. Therefore, it was necessary to study the components common to both setups as well as the interaction of both systems. Some basic component properties of the original Grande station setup, which are relevant for the commissioning of the new FADC-based system, are discussed within the following sections.

3.1 Photomultiplier tube (PMT) configuration of a Grande station

Each Grande detector station is equipped with a total scintillator area of $10\,\mathrm{m}^2$, divided into sixteen quadratic plates (sized $80\times80\,\mathrm{cm}^2$). Separate pyramidal light guides are attached to each of the plates from below; photomultiplier tubes are mounted at the other end of the light guides. The innermost four detector cells are equipped with two PMTs (one configured for high amplification, one adjusted to a lower amplification factor), while each of the surrounding twelve scintillator cells is monitored by a single photomultiplier tube operated in high gain mode.

The gain of the photomultiplier tubes[1] is adjusted by means of the dynode and anode voltages. For a given voltage, the amplification factors of different PMTs of the same type usually differ noticeably; in order to achieve the same gains for all tubes, it proved necessary to supply them with different voltages. For this reason, the Grande stations were equipped with programmable voltage dividers, which allow to adjust the voltages individually, independent of the main high voltage supply located inside the central DAQ station. One way to achieve equal gains for the PMTs is to adjust the respective supply voltages in such a way, that all high gain and all low gain PMTs respectively, generate pulse signals of the same height for scintillation light of the same intensity.

The photomultiplier tubes, operated in low gain mode, are supplied with voltages

---

[1] Photonis XP3462 or compatible

Property	**Value**
no. of stages ($\equiv$ no. of dynodes)	8
spectral range	290 nm–650 nm
maximum sensitivity	@ 420 nm
supply voltage range	1150 V–1600 V
absolute maximum supply voltage	2000 V
absolute maximum anode current	200 μA
gain	$\approx 10^6$ @ 1350 V
mean background noise frequency	5000 Hz–10000 Hz
mean anode sensitivity deviation	-0.2 %/K @ 400 nm ($0 \leq T \leq 40\,°C$)
anode pulse	
rise time	3 ns @ 1600 V
duration at half pulse height	4 ns @ 1600 V
parasitic anode$\leftrightarrow$dynode capacity	5 pF

Table 3.1: Some characteristics of the photomultiplier tube [27].

ranging from 1200 V up to 1600 V, resulting in amplification factors of 10% compared to that of PMTs supplied with voltages ranging from 1500 V up to 2000 V for high gain operation. Some characteristics of the photomultiplier tube used for the Grande stations are listed in table 3.1.

The current signals of the individual PMT anodes are converted to voltage signals by means of 50 Ω resistors, which are acting as transmission line terminations for the attached coaxial cables at the same time. The pulse signals of the PMTs are transmitted to the pulse mixer module via those cables; in order to achieve the same signal delay for all PMTs, it is mandatory to install coaxial cables of the same length.

3.2 The PMT pulse mixer

The characteristics of the photomultiplier pulse mixer, being the first stage of the whole module chain, have strong impact on the performance data of the entire original Grande data acquisition system. Since the signal for the FADC-based system is intercepted right at the output connector of the pulse mixer module, its characteristics also affect the performance data of the new DAQ system. Due to the fact, that the FADC-based system offers additional information on air shower events by performing high resolution digitizing of the PMT pulse signals, it is especially sensitive to e.g. signal distortions, which lead to a loss in data quality.

3.2.1 Internal structure of the mixing device

Pulse mixing is accomplished separately for high gain and low gain photomultiplier tubes, respectively. That is, there is one pulse mixer module dedicated for handling low gain

PMT signals, whereas high gain PMT signals are processed by another pulse mixer module.

The PMT pulse signals are mixed passively inside the mixer module; i.e. resistor networks are used for combining the four low gain source signals to a low gain sum signal. The same applies to high gain source signals, for which the sum signal is formed by the sixteen high gain input signals. Mixing the source signals in a passive way has several implications. Since there are no additional active components involved in the signal mixing, the Johnson-Nyquist noise (i.e. the thermal noise) of the resistor networks is the only noise contribution of the mixer module. However, the passive mixing results in a signal degradation by about 88.7% (corresponding to an attenuation of 19 dB) according to SPICE simulations conducted for a coarse model—see figure 3.1. And finally, there is no easy way to distribute a passively mixed sum signal to multiple DAQ systems without employing additional active components like e.g. the "Active Probe" device presented in appendix D.

3.2.2 Analysis of the mixer device using SPICE modeling techniques

The SPICE model of the mixer module is shown in figure 3.2. Only the components, which are taking part in the actual PMT pulse signal mixing, have been included. The SPICE simulator was used to perform a frequency sweep analysis on the circuit model; that is, it gradually increased the frequency of the sine wave stimulus, while evaluating the output amplitude and phase shift with respect to the stimulus. The results gathered by conducting the analysis are presented in figure 3.1.

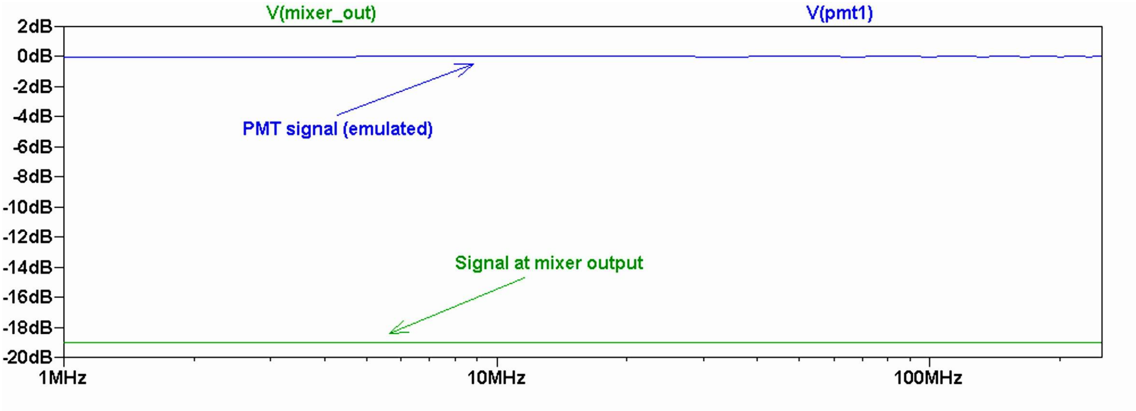

Figure 3.1: Signal amplitude degradation vs. frequency caused by passively mixing PMT input pulses. The individual PMT pulse signals experience amplitude losses of approximately 19 dB. On the other hand, the spectral transfer characteristics of the mixer device are not noticeably depending on the frequency due to the passive way of mixing. The phase shift information has been omitted in this figure, since it does not matter for the estimation of signal amplitude degradation.

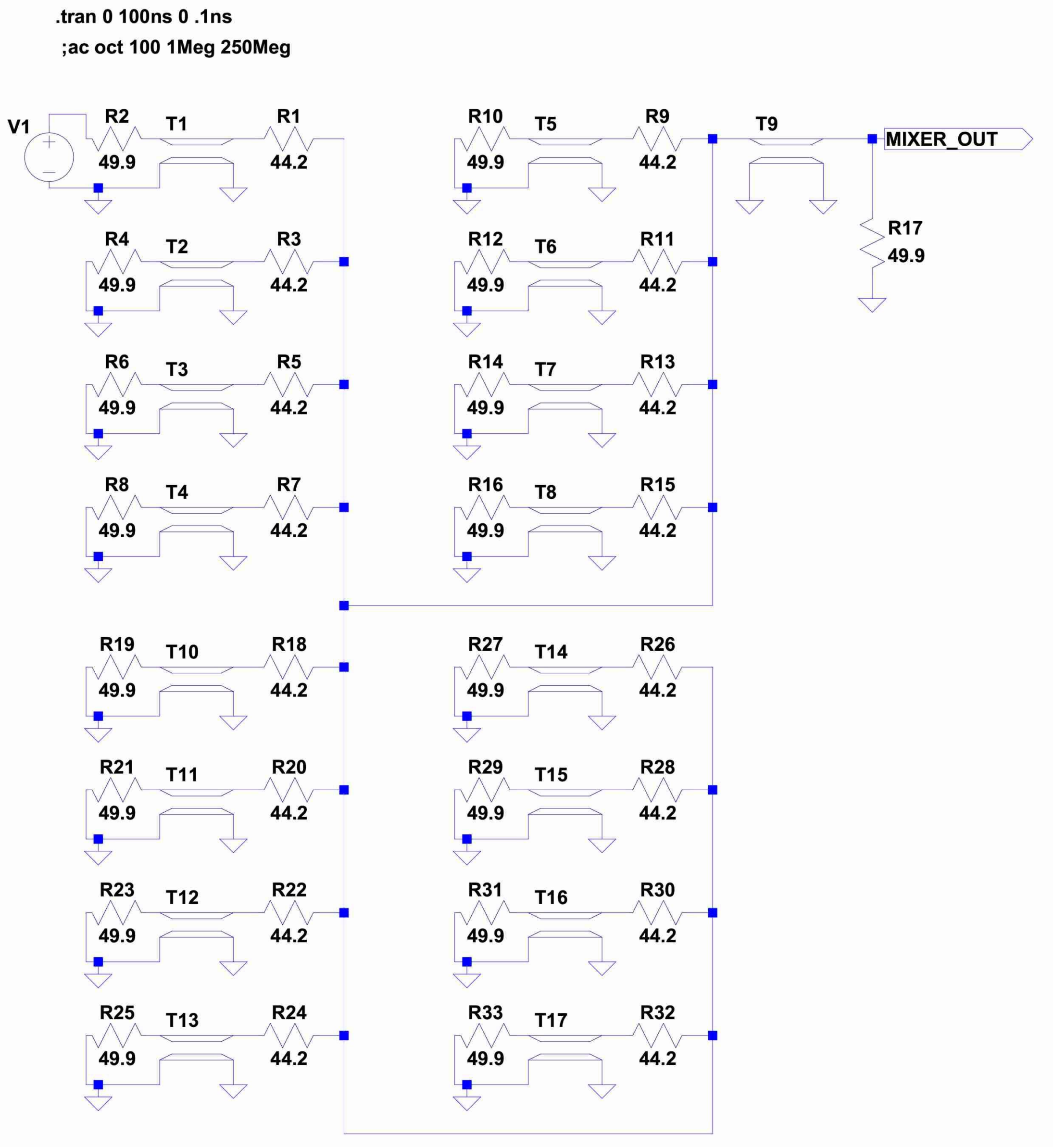

Figure 3.2: A coarse SPICE model of the PMT pulse mixer. Components apart from the actual mixing parts are not shown. The generator object V1 is injecting a PMT pulse stimulus (see appendix A) into the mixer device. Only one attached PMT is simulated by the setup; this can be done without any loss of generality, since all PMT input circuitries are identical for the model presented as well as for the real hardware device; moreover, in most cases, vertically incoming single particles are hitting only single scintillator cells of a Grande station at a time. Thus, usually only one PMT at a given time is sensing a light pulse for single particle events. Otherwise, the pulse signals of individual PMTs undergo an undisturbed superposition, i.e. they are just added up without feedback on the remaining tubes.

3.3 The shaping amplifier

In the original Grande setup, the PMT pulse mixer device feeds the pulse shaping amplifier with the summed PMT pulse signals. Since the signal for the new FADC-based data acquisition system is obtained by spying on the connection of the PMT pulse signal mixer and the corresponding shaping amplifier, it is vital to gain knowledge on the input properties of the latter and the actual feedback on its input signal as a consequence of those properties.

3.3.1 The structure of the pulse shaping amplifier

The transfer characteristics of the shaping amplifier unit are of no concern to the FADC-based DAQ system, since the output signal is solely evaluated by the peak sensing ADC units of the original Grande DAQ setup; it is, however, not used at all by the new FADC-based system. The shaping amplifier is used for integrating and shaping the PMT pulses summed by the mixing device; thus information on the actual pulse shape development of the individual photomultiplier tubes in time are lost, making it useless for the FADC-based system, which is capable of processing the time development information.

The shaping amplifier includes a charge integrating input circuitry, which is configured for an $8\,\mu$s integration period. The resulting integrated waveform is then amplified and converted to match the $50\,\Omega$ impedance of the coaxial cables used for the transmission of the integrated signals to the peak sensing ADC modules inside the central Grande DAQ station. By using shaped signals, it is possible to transmit information on the charge measured on a distance of up to 700 m, which is about the maximum distance between the Grande array stations and the central Grande data acquisition station.

3.4 Interaction of the PMT pulse mixer with the pulse shaping amplifier

Figure 3.3 shows a schematic overview of a model used to explore the interaction of the PMT pulse mixer and the corresponding shaping amplifier in comparison to a PMT pulse mixer terminated by a pure Ohmic resistance. Hence, the model, which has been composed of sub-models of the pulse shaping amplifier, the PMT pulse mixer and the PMT pulse source, eventually provides an insight into the signal modifications caused by the pulse shaping amplifier.

Since the input circuitry of the digitizer subsystem basically behaves like an Ohmic resistance with respect to the signal source (see p. 61, figure C.1), the results gathered from the respective branch of the simulation model provide information on the pulse shape to be digitized by the KGEMD board in a setup, where the KGEMD is operated exclusively, i.e. with the original Grande DAQ system detached. In contrast, the upper branch of the model's schematic diagram represents the situation for concurrent operation of both Grande data acquisition systems; in this case, the connection of the pulse shaping amplifier and the corresponding PMT pulse mixer is tapped to obtain the input signal for the digitizer subsystem KGEMD.

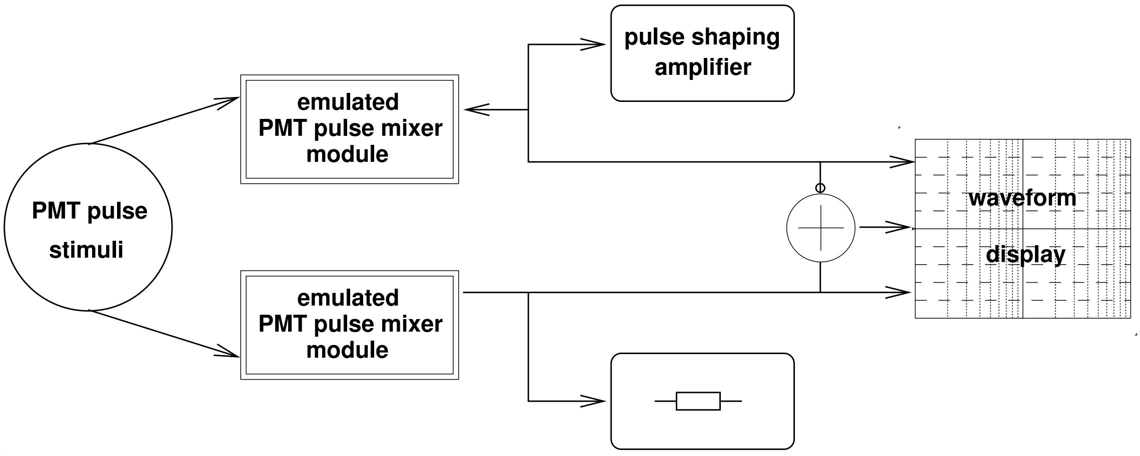

Figure 3.3: Setup for an analysis of the mixer-shaper interaction. The source unit on the left provides identical PMT-like stimuli to both simulation branches of the model. The branches are constructed from sub-models in a symmetric way except for the different signal sinks; the upper branch is terminated by the model of a shaping amplifier, whereas the respective task is fulfilled by the model of an Ohmic resistance for the lower branch. The voltage signals evaluated at both the shaping amplifier's input stage and across the Ohmic resistance as well as their differential signal are then shown on the waveform display of the SPICE simulator (see figure 3.4). The current fed back into the mixer device is indicated by the arrow directed from the shaping amplifier back to the mixer device.

3.4.1 Impact of the shaping amplifier's feedback on the mixer signal

The shaping amplifier, being a device with a non-linear, low impedance input stage, causes a current, that is fed back into the mixer device. Thus, the pulse signal waveform is undergoing modifications. The digitizer subsystem (KGEMD) of the FADC-based DAQ system is, however, reading this modified signal via an intercepting "Active Probe" device (see appendix D). Running a simulation on the model shown in figure 3.3 for a typical stimulus results in a waveform display as presented in figure 3.4.

If there were no signal modifications caused by the pulse shaping amplifier, the amplitude of the deviation signal in figure 3.4 would be zero. However, due to the shaping amplifier's non-linearities, the deviation signal is a non-zero signal. The deviations of the pulse shapes do not result in a large deviation in terms of the respective integrals in time, though; the integrals of the pulses in figure 3.4 differ from one another by approximately 2%. Therefore, the FADC-based data acquisition system is able to determine particle energies from the pulse shape information without any additional compensation for the shaping amplifier's impact. The error caused by quantization due to the analogue-to-digital conversion inside the KGEMD units reaches the same order of magnitude as for event pulse signals detected for a far distant shower core [24].

In contrast, in order to be able to retrieve information beyond particle energies from the pulse shapes recorded by the digitizer subsystem, it is necessary to get rid of the shaping amplifier's impact by compensating for it.

3.4.2 Compensation for the pulse shaping amplifier's impact

The impact of the pulse shaping amplifier's input circuitry can be eliminated or reduced by one of the following measures.

1. Deployment of pulse signal splitter units inside all Grande stations in order to decouple the DAQ systems.
2. Implementation of a compensating network into an intercepting device, e.g. an "Active Probe" device modified to provide the KGEMD unit with a corrected signal.
3. Detachment of the original Grande data acquisition system, including the pulse shaping amplifier; in order to operate the new FADC-based system exclusively as a replacement DAQ system.
4. Digital post-processing of the event pulse information read by the FADC-based DAQ system in order to correct for the pulse shape modifications caused by the pulse shaping amplifier.

At the moment, the first and the second item are not an option, since "Active Probes" of the type described in appendix D have been installed already; therefore, these items would require additional research and hardware development efforts and, subsequently, 74 of those units would have to be replaced. Moreover, the detachment of the original Grande DAQ system is currently neither feasible nor desirable, since it has reliably been taking data for a long time already, although it is lacking some additional shower event information, which the FADC system is capable of providing.

Thus, further efforts have been made to compensate for the impact of the pulse shaping amplifier on its input signal by means of digital post-processing. By applying a discrete Fourier transform to the pulse shape information (see figure 3.4), which results from the simulation branches of the model presented in figure 3.3, the spectral contributions of the waveforms have been calculated within the frequency range limited by the Nyquist frequency—see figure 3.5. The uniform characteristics of both the unmodified signal spectrum and the spectrum modified by the impact of the pulse shaping amplifier suggest, that the signal impact can be corrected for by compensating for the spectral modifications using a fixed projection function.

From the spectral distributions shown in figure 3.5, the projection function can be constructed. First, the ratio of the spectral distribution has been evaluated. A non-linear regression algorithm was then applied to the resulting data; see figure 3.6. The modified spectrum can be converted into the unmodified one by multiplying it with a projection function like

$$p(f) = a_0 + a_1 f + a_2 f^2. \tag{3.1}$$

Here, the regression algorithm yields the following parameters:

$$\begin{aligned} a_0 &= 0.98172, \\ a_1 &= 1.1569 \cdot 10^{-9}\mathrm{s}, \\ a_2 &= -4.1783 \cdot 10^{-17}\mathrm{s}^2. \end{aligned}$$

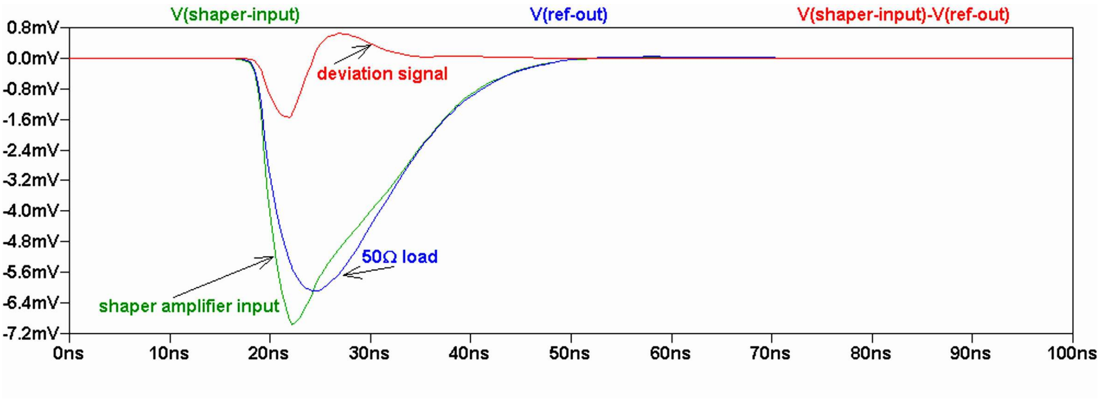

Figure 3.4: Signal impact caused by the shaping amplifier. A typical PMT-like stimulus (see appendix A) has been used for the simulation according to the schematic model in figure 3.3; the figure above actually shows the contents of the waveform display for that model. The pulse signal, that has been evaluated for the 50 Ω load (which is equivalent to one digitizer channel of a KGEMD board) corresponds to the stimulus pulse shape and has only been degraded linearly (see figure 3.1) by approximately 19 dB in comparison to the signal source amplitude. The mixed PMT-pulse signal originating from the simulation branch containing the model of the shaping amplifier, however, has been modified by the input stage of that component; the deviation signal results from the differential signal of the two branch signals and has been added for illustration.

The standard deviation for the regression was $\sigma = 0.02$.

Figure 3.7 shows the results of applying the spectral projection mentioned above to waveform data. First, the waveform has been transformed to the frequency domain using a (forward) discrete Fourier transform (DFT); thereafter, the spectral projection function was applied to all the samples in the frequency domain. Eventually, those samples were transformed back into the time domain by applying a backward DFT [25].

The compensated pulse shape does not match the original, i.e. unmodified waveform at the first slope. The slope is not as steep as for the original waveform by far and the pulse is widened up towards the left of the plot. However, one drawback of the pulse stimulus used for the simulation is the fact, that the first order derivative of the underlying function exhibits a discontinuity at that time. The discontinuity causes contributions to the high frequency region of the respective spectrum, which are lost after the discrete forth and back fast Fourier transform (FFT) due to the Nyquist frequency limitations. Real signals will therefore not exhibit such a widening.

Since the internal structure of the pulse shaping amplifier is currently not known completely, it cannot be decided conclusively, whether the SPICE model really complies with the real shaping amplifier, i.e. the hardware device, in every respect. In order to investigate this issue further and to ensure the compliance in the end by refining the model, the response of the hardware device has to be evaluated and compared to the results from the simulation; however, for this purpose, the real pulse shaping amplifier has to be fed with a stable m.i.p.-like pulse shape—just like in the simulation. So far, it has not been possible to conduct the measurements necessary using the equipment available.

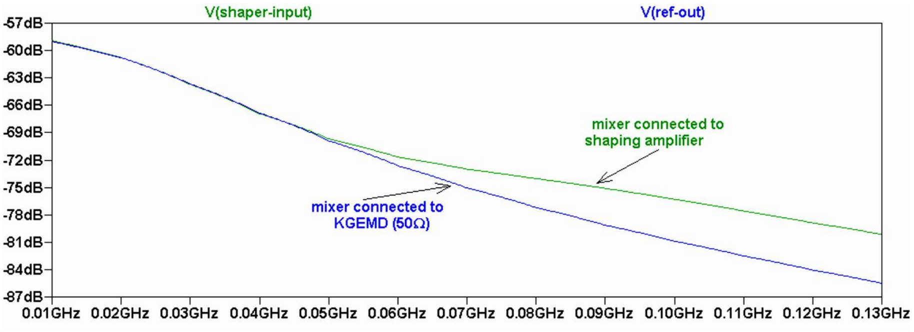

Figure 3.5: Spectral modifications caused by the pulse shaping amplifier. Each of the waveforms evaluated for the input section of the shaping amplifier and across the Ohmic resistance in figure 3.4, i.e. the loads of the simulation branches in figure 3.3, have been transformed into the frequency domain using a discrete Fourier transform (DFT). Only the frequency range up to the Nyquist frequency of the digitizer subsystem KGEMD has been taken into consideration.

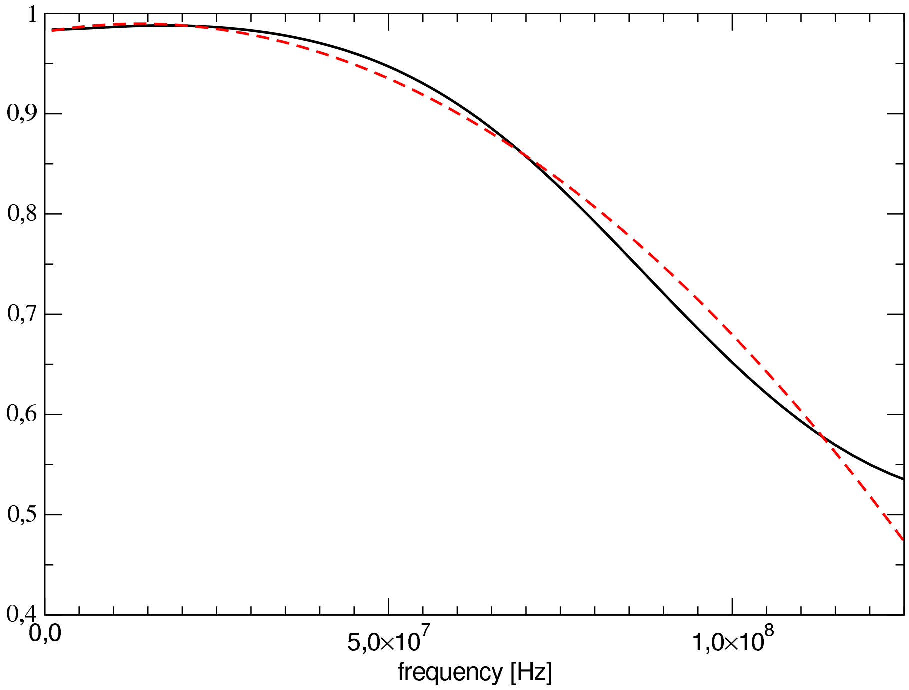

Figure 3.6: Spectral projection function and quadratic fit. The projection function (solid line) has been evaluated as the ratio of the spectral distributions in figure 3.5. A quadratic fit algorithm has been applied in order to obtain a functional description (dashed line).

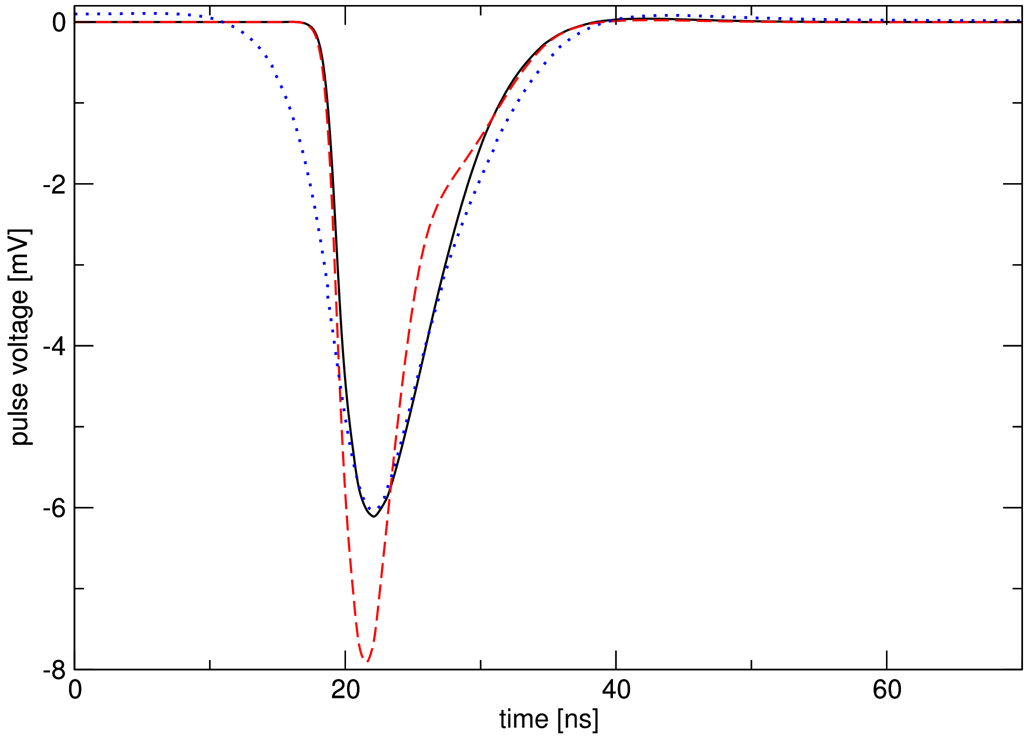

Figure 3.7: Input signal of the pulse shaping amplifier prior (dashed line) and after digital post-processing (dotted line), respectively. Post-processing has been accomplished by applying a forward DFT to the waveform data in figure 3.4, followed by a backward DFT; the spectral composition of the pulse has been corrected just before the backward transform by the function in figure 3.6, which has been determined from the spectral distributions shown in figure 3.5. The signal across the 50 Ω load is shown for comparison (solid line).

Chapter 4

The FADC-based DAQ system in the Grande array

The original Grande data acquisition system suffers from several drawbacks. Everytime a cluster is signaling a coincidence condition (4/7 or 7/7 coincidence) or an external source is generating a trigger signal, the Grande DAQ system initiates a data read-out. As long as the read-out is in progress—this takes about 500 μs—the detection of shower events is disabled, i.e. the system is not able to process any additional air shower events occurring during this dead time.

For calibration purposes, single particle spectra are acquired from each of the Grande stations; hence, the mean energy deposit of a minimum ionizing particle can be assigned to a specific value obtained during the DAQ read-out. With the original Grande DAQ system, those spectra cannot be acquired on the fly. Instead, the acquisition of air shower events has to be interrupted to obtain single particle event data, since all but the station, for which spectral data shall be collected, are masked in the trigger. Thus, taking single particle event data for a single Grande station results in additional 250 μs of dead time. For the current configuration, three single particle events are recorded after each shower event.

Furthermore, the event data of a particular scintillation detector station is processed separately for each set of high gain and low gain PMTs, respectively. The transmission to the central Grande DAQ station is accomplished via coaxial cables. As a consequence, each detector station is equipped with shaping amplifiers, which perform an integration of the PMT pulses during a period of 8 μs; the amplitude of the amplifier's output signal is proportional to the measured charge, which in turn is proportional to the deposited energy. The amplifier output signals are barely attenuated on their passage through the coaxial cables due to their relatively low frequency. Inside the central Grande DAQ station, the integrated signals are received by peak sensing ADCs, which retrieve the measured charge integral by sensing the amplitude of the particular incoming signals. Additionally, TDCs perform the measurement of particle arrival times; the signals originating from discriminator units in the Grande array stations are used for this purpose and allow the determination of the first incoming particle's arrival time for each station. Thus, only the time of the particle incidence as well as the total deposited energy are recorded by the original Grande data acquisition system, whereas information on the development in time of the PMT pulses is lost.

Since a complex chain of modules is used to implement the original DAQ system's functionality, it is vulnerable to malfunctions of individual units. After replacing defective units, the need for recalibration arises in many cases, resulting in additional system downtime or partially invalid data otherwise.

4.1 The FADC-based Grande DAQ system

In order to get rid of the drawbacks mentioned above, a FADC-based data acquisition system has been developed and built at the University of Siegen. It aims at acquiring air shower data virtually free of dead time, while providing detailed PMT pulse shape information at the same time. Moreover, it provides all prerequisites for enhancing the resolution regarding time and energy compared to the capabilities of the original Grande DAQ system; and by design, the FADC-based DAQ system enables the operating software to implement a wide variety of trigger conditions. Some specifications and information on the performance data concerning the FADC system are listed in table 4.1.

4.1.1 Components of the FADC system

The components, from which the FADC-based DAQ system is made, are installed partly inside each of the Grande stations, partly inside the central Grande DAQ station, which is housing the original Grande DAQ setup as well.

Each of the 37 Grande array stations has been equipped with the following components:

- one digitizer board (KGEMD), enclosed in a metal box (serving as shielding against electromagnetic interference);
- two active probe units, providing the KGEMD board with intercepted PMT pulse signals supplied by the high gain and low gain PMTs, respectively;
- one power supply unit, feeding both the KGEMD board and the active probe units with filtered and stabilized electrical power, drawn from the NIM power supplies inside the Grande stations.

The Grande station setup has not been altered in order to incorporate the enumerated components except for the connection of the PMT sources and the respective shaping amplifiers making up the input stages of the original Grande DAQ system. The active probe units (see appendix D), however, transparently intercept the PMT pulse signals while retaining the original cable connection, i.e. with a neglectable impact on the data taking of the original DAQ system.

The following subsystems have been installed inside the central Grande DAQ station in order to receive and process the data transmitted by the KGEMDs of the Grande array stations:

- five storage boards (KGEMS), installed inside a VME crate. The KGEMS boards receive the digitized data from the KGEMDs installed in the Grande array stations, each board can handle up to eight input channels;

- five first level PCs, each containing one KGEMP board, which establishes the link between one KGEMS board and the corresponding first level PC;
- one master PC, connected to the first level PCs via ethernet network;
- a trigger receiver card (KGEMT), installed inside one of the first level PCs in order to receive trigger signals generated by one of the main KASCADE trigger sources.

4.1.2 The digitizer component (KGEMD)

Each Grande array detector station is equipped with a KGEMD board. The KGEMD is capable of simultaneously digitizing the pulse shape information originating from both the high gain photomultiplier tubes and their low gain counterparts. Actually, the mixed signals of all sixteen PMTs operated in high gain mode and the mixed signals of the four low gain photomultiplier tubes (monitoring the innermost scintillator cells), respectively, are used. These mixed signals are already in use by the original Grande DAQ system; thus, active probe devices, which enable the KGEMD boards to transparently intercept those signals, had to be deployed.

The digitizing of the mixed PMT pulses takes place all the time. As long as the high gain input signal does not exceed the threshold of the particular KGEMD board, the digitized data is just discarded; the threshold of an individual KGEMD can be set by programming the corresponding reference DAC on the digitizer board accordingly. The KGEMD boards do not require an external trigger source due to the built-in comparator, which can be programmed to initiate data acquisition at an arbitrary level. On crossing the preset threshold, a data packet is formed including a “magic word” (announcing KGEMD data), a board number (unique to the particular KGEMD board), multiplexed high gain and low gain pulse shape data, followed by three time stamp counter values incremented by the main KASCADE 1 Hz and 5 MHz clock sources (received from the KASCADE time stamp distributor via optical links) and the 62.5 MHz clock reference (internally generated by a crystal onboard the KGEMD PCB). In order to ensure data integrity of the optical high speed link, which is used for the data transmission to the DAQ station on a distance of up to 700 m, a CRC-based error detection mechanism has been implemented in the FPGA core logic [19], appending meta data to the data stream.

Pulse shape data of up to 48 ns before the high gain signal was exceeding the preset threshold can be included into the data stream because of the FADC component[1], which is equipped with an output queue, thereby providing a data delay. Due to the data queuing, up to twelve digitized data samples actually prior to the trigger time are included into the data stream to form the event data packet. Although the digitizing period is limited to 1.008 μs, it may repeatedly be prolongued by another digitizing period of the same duration in case the preset threshold is crossed once again during the last 100 ns of the current period. See figure 4.1 for an overview of the conceptual design of the KGEMD.

A set of FIFO registers onboard the KGEMD board and inside the main FPGA enables the digitizer logic to perform up to four additional digitizing periods even while the transmission of the first data packet is still in progress.

---

[1] Analog Devices AD9238

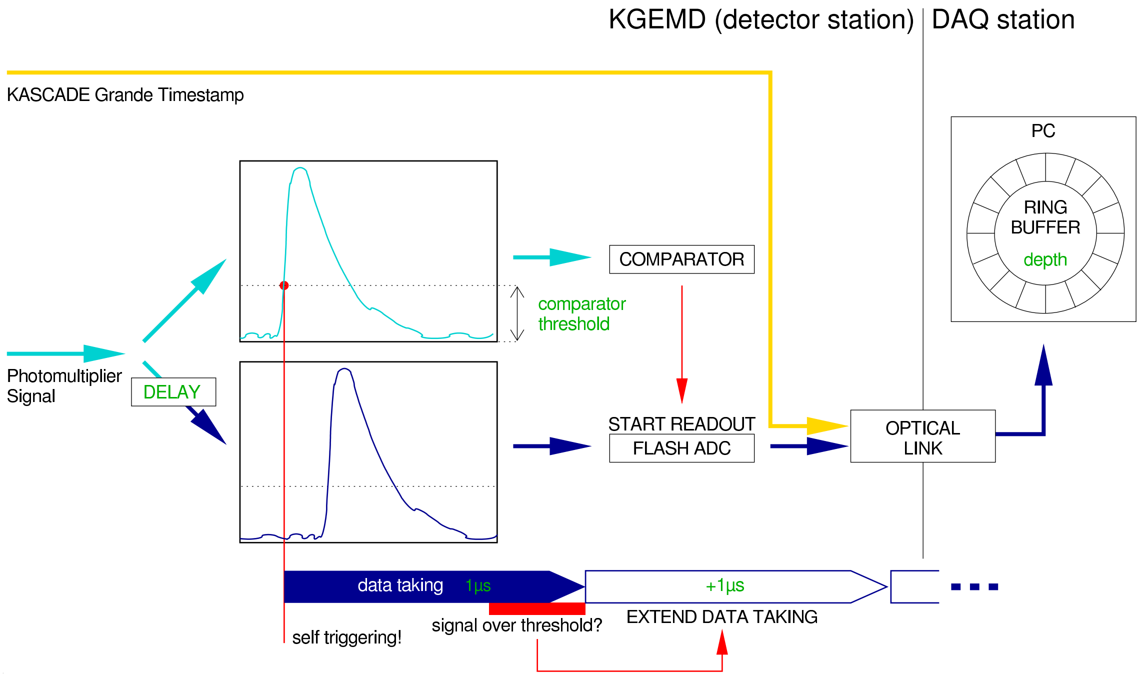

Figure 4.1: Conceptual design of the KGEMD unit. The low gain channel has been omitted for reasons of clarity, since it does not contribute to the self-triggering or prolongation of digitizing periods. The digitizing of low gain pulse shapes is done exactly the same way as for the high gain channel; the two data streams are simply multiplexed in order to share a common data packet. The FADC-system related equipment of the central Grande DAQ station is only roughly denoted on the right side of the figure [1].

4.1.3 The storage board (KGEMS)

The data digitized by the KGEMDs is transmitted to five KGEMS boards inside the central Grande DAQ station via optical fibres. Due to the distance of up to 700 m between the DAQ station and the most distant Grande detector stations, single-mode fibres have been installed for the high speed links. Multi-mode fibres are in use for the time stamp clock distribution [20], though, since the respective signals are relatively slow (minimum light pulse duration ≈200 ns compared to ≈800 ps for the data link) and the signals are periodic, i.e. there is no impact on the eye width of the optical time stamp clock transmission. In general, however, multi-mode fibres are not suitable for data transmissions over large distances; at a speed of 1.2 Gbit/s (corresponding to the 800 ps pulse width of the optical data transmission for the FADC-based data acquisition system), the transmission is typically limited to distances of about 500 m for multi-mode fibres.

The KGEMS board is sometimes also referred to as the “receiver board”, since it is equipped with eight optical receivers. Hence, it can handle data streams of up to eight digitizer boards, each installed in one of the Grande detector stations. On the transmitter side, the data packets to be transmitted to the central DAQ station have been serialized, i.e. transformed into a serial data stream of single bits, and control information has been added. On the receiver side, the control information is stripped off and the data packets are retrieved by the receiver chip. The data words received by individual channels are transferred into separate FIFO registers, which are capable of buffering 31 event data

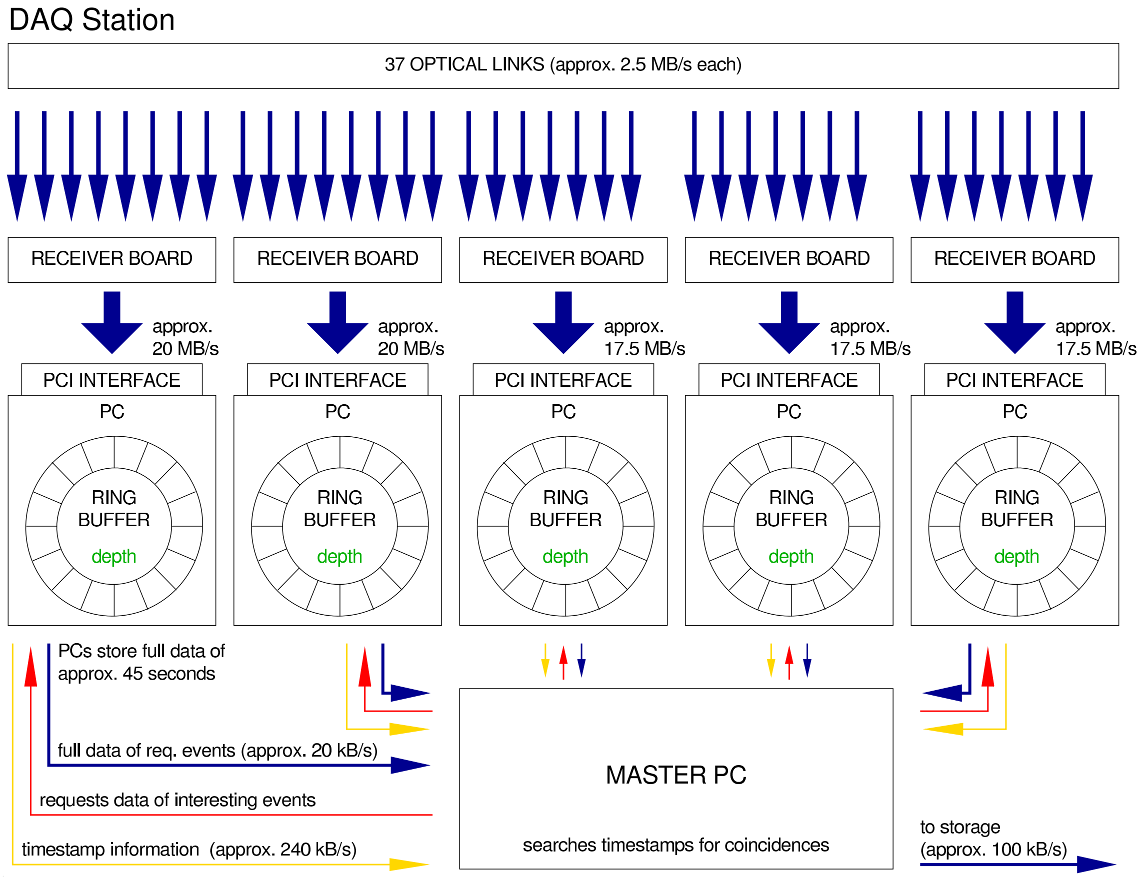

Figure 4.2: Overview of the functional units of the FADC-based data acquisition system. Only components located inside the central Grande DAQ station are shown. The internal data flow is indicated by arrows, air shower data coming in from the KGEMD boards inside the Grande stations via optical links are depicted by the upmost arrows. Multiple data connections between the master PC and individual first level PCs are routed through common physical network links. The KGEMT card, which is used for the reception of external KASCADE trigger signals, is not shown in the sketch; however it is installed and operated in one of the first level PCs [1, 19].

packets each. The contents of all FIFO registers are then multiplexed and fed into a FIFO, which can temporarily store up to 127 event data packets. The resulting data stream is converted to 32 bit LVDS signals and transmitted to the KGEMP card of a first level PC using a shielded standard SCSI cable.

The five KGEMS boards are installed inside a VME crate, which provides the power supply as well as a control interface (using the VME protocol). The VME interface can be used in order to perform control operations, e.g. disabling/enabling receiver channels under software control despite their link status, requesting status information etc.; it is even possible to inject data into the KGEMS for testing purposes or to read FIFO contents via the VME bus. Compared to the data transmission via LVDS, the latter transmission mode is rather slow and therefore it is only suitable for diagnosis.

4.1.4 The PCI interface card (KGEMP)

The KGEMP card actually consists of two cards. First, a commercial prototyping PCI interface card built around a standard PCI controller chip[2] and, second, an additional custom-made board, mounted in a 'piggyback' fashion, which provides a synchronous 32 bit LVDS interface to be connected to one of the KGEMS boards. The onboard 32 bit wide FIFO, which can hold up to 31 event data packets (each containing 1024 bytes of event data and 8 bytes of meta data for error detection), provides enough additional buffer space in case of the first level PC being temporarily too busy for flushing the buffers [21]. The PCI controller has been setup for asynchronous transfer mode and contains a FIFO of its own, which can only buffer a few words of data, however, and is mainly intended to sustain high data throughput during DMA data transfers.

4.1.5 KGEMT, the trigger receiver card

The main purpose of the KGEMT is the reception of trigger signals issued by the KASCADE main trigger sources. Whenever the KGEMT receives a trigger pulse, the master PC may read out the event data originating from all KGEMDs, which detected a particle incidence at nearly the same time.

Another feature of the trigger receiver card is the built-in GPS receiver. Although it is possible to use the GPS component for assigning absolute time values to the arbitrary time stamp counter values, this feature of the KGEMT is currently disabled, since the time synchronization via the network time protocol provides sufficient accuracy [19].

4.1.6 First level PCs

Five first level PCs are installed inside the central Grande DAQ station; each of them is equipped with a KGEMP card, which in turn is acting as the data sink for one of the KGEMS boards. Under control of the operating software of the first level PCs, the KGEMP is set up for DMA transfers of event data packets into a region of the computer's main memory. This memory region constitutes a ring buffer. Thereby, each first level PC, being equipped with 1 GB of main memory, is capable of keeping up to 900,000 events at the same time.

The first level PCs send a list of time stamp values of event packets received and the corresponding unique KGEMD board numbers (which translate to Grande station numbers) to the master PC. The master PC can in turn request the complete waveform data of specific events; usually the master PC will receive an answer to its request containing the pulse shape data; only on rare occasions, the particular data packet may no longer be available inside the ring buffer of the respective first level PC, because it has already been expunged by new data packets. This could e.g. happen, if the first level PCs continuously receive data streams at high speed and the master PC is not capable of processing the resulting time stamp data streams due to a lack of processing power. See figure 4.2 for an overview of the data flow. Moreover, the first level PCs can continuously perform numerical pulse shape integration in order to obtain energy spectra for all connected stations.

---

[2] AMCC S5933 resp. S5935

4.1.7 The Master PC

The event builder software, which is running on the master PC, receives all time stamp information of the event packets received by the five first level PCs. Thus, the master PC actually receives full information on events detected within the Grande array by means of its network connections to all of the first level PCs. In case the master PC finds coincident energy deposits for a number of detector stations, it can request the digitized waveform data of stations involved at a specified time by sending appropriate commands to the first level PCs. The event data packets gathered for a particular air shower event are stored on hard disk for further analysis. The event finding strategy depends on the software routines implemented in the event builder software running on the master PC; part of the FADC system's flexibility and uniqueness results from the software implementation, which supersedes hard-wired or hard-coded event building.

4.2 Conclusions

The extensive buffering scheme, used by the FADC-based data acquisition system in order to sustain high data rates without losing event data, implies, that the event data is actually queued. Thus, the data is subject to delays until the event building takes place. For this reason, the FADC-based data acquisition system cannot supply any other components of the KASCADE-Grande experiment with trigger signals, because the air shower event is usually long gone, when the FADC-based system recognizes a coincidence of particle detections within Grande array stations. However, the FADC-based system has been designed as a stand-alone DAQ system anyway. Moreover, the original Grande DAQ system is providing a trigger signal already.

By design, the FADC-based data acquisition system, which has been installed in the Grande array, offers several advantages:

- operation free of dead time is achieved by extensive multi-stage buffering throughout all components of the DAQ system;
- the high sampling rate of 250 MHz in conjunction with 12 bit signal resolution provides detailed pulse shape information. By applying methods of digital signal processing to the waveform data, e.g. filtering or noise suppression, further shower parameters may be extracted from the development in time of the PMT pulses;
- due to the self-triggering, the digitizer units installed in the Grande array do not rely on external trigger sources;
- the acquisition of energy spectra for each Grande station is accomplished on the fly, i.e. without interrupting the acquisition of air shower events;
- since the event building is done entirely by software programs, a wide variety of trigger strategies may be tested without the need for rewiring any trigger logic;
- it is possible to operate the new FADC-based DAQ system and the original Grande DAQ system concurrently. Hence, the new FADC-based system can supply the original DAQ system with valuable cross-calibration data.

Property	**Value**
digitizer type	FADC, 4-fold time-interleaved
digitizer resolution	12 bit
digitizer sampling frequency	250 MHz
total digitizing period	1.008 μs (may be prolongued by additional 1.008 μs periods)
no. of digitizer channels per KGEMD	2
digitizer input voltage range	-1…0 V
trigger threshold resolution	12 bit
resolution of KASCADE time stamp signals	1 s, 200 ns
internal KGEMD time stamp resolution	16 ns
KGEMD→KGEMS link capacity	$\approx 1.2 \cdot 10^5$ events/s
link types	
KGEMD→KGEMS	1300 nm single-mode fibre
time stamp distributor→KGEMD	800 nm multi-mode fibre
KGEMS→KGEMP	32 bit LVDS
KGEMP→first-Level-PC	32 bit PCI
first level PC→master PC	Ethernet network (100 Mbit/s)
event buffer depths	
KGEMD	5 events
KGEMD→KGEMS	8 channels × 31 events
KGEMS→KGEMP	127 events
KGEMP	31 events
first level PC	$9 \cdot 10^5$ events
event data packet size	1032 bytes (including 8 bytes of meta data for error detection)
expected data packet rate per station	$\approx 2500\,\mathrm{s}^{-1}$

Table 4.1: Properties of the FADC-based DAQ system.

Chapter 5

Parallel operation of both Grande DAQ systems

5.1 Signal interception vs. signal splitting

There are three main methods for operating data acquisition systems in parallel: by multiplexing, intercepting or splitting the input signals.

If an experiment allows to foresee the time of the event to be processed, a multiplexing unit may be used in order to select between the DAQ systems. That is, a connection of the detector to the respective data acquisition system is established right before the event will be detected; as a consequence, the DAQ systems are really taking data alternately rather than in parallel. For example, if the DAQ systems are to be used in conjunction with a particle accelerator facility, the time of the event to be detected at the target's location may be estimated by the pulse that is applied to a kicker magnet or a similar device (plus a time delay caused by the particle propagation).

In the case of an astroparticle experiment like KASCADE-Grande though, it is hard to determine the right time for establishing the connection between the particle detector and one of the DAQ systems. Some kind of top layer particle detector could sense the energy deposit of a particle passing through it and probably hitting the main detector later on; but this is not applicable to the Grande stations and can therefore not be considered an option. Furthermore, the events of main interest for this experiment are those where particles carrying extremely high energies (see section 1.1) are hitting the detector array; events like those are rare, though, (about 80 events per year for energies exceeding 10^{18}eV). Multiplexing the detector signals between the DAQ systems in order to operate them in an alternating fashion, would further reduce the number of the most interesting events by about 50% for each of the two DAQ systems.

In addition, the FADC system, being a dead-time free system by design [1], would suffer noticeably from the dead-time caused by the signal multiplexing. Introducing a multiplexing device into the signal path between the detectors and the DAQ systems would moreover add additional noise to the signal provided by e.g. the PMTs in the Grande stations comparable to the noise introduced by a splitting solution (see below).

One of the advantages in operating both systems for data taking in the Grande array simultaneously (in contrast to alternately taking data) is the possibility of cross-calibrating the systems, e.g. with respect to the energy calibration; in addition, because of the KGEMT card, the original Grande system may supply trigger cluster signals to the FADC system which is working as a self-triggering system otherwise. Consequently, there is no use in choosing a multiplexing unit for taking data alternately.

There are, however, two other ways to operate DAQ systems from the same signal source.

First, the connection between the source and the original DAQ system may be kept; an additional device "spying on" (i.e. intercepting) the transmission is providing the other DAQ system with the source signal. Using this technique, the impact of the additional DAQ system on the original signal path is minimized, i.e. the original system is receiving the source signal virtually undistorted. Depending on the circuitry at the input of the original system, the DAQ system operated in addition may receive an input signal, that differs from what it would be supplied with if operated exclusively.

Second, all the DAQ systems being operated in parallel may be supplied with signals from a splitting device, i.e. a device equipped with one input channel, distributing the source signal to its output channels using some kind of amplifiers. Thus, the DAQ systems connected to the splitting device receive signals independently of each other; the signal for the original DAQ system is provided the same way, however. As a matter of fact, the impact of the active components, which make up the splitting unit, may prevent the original system from properly processing event signals due to impedance mismatches or extra noise.

5.2 Techniques for signal interception

Two methods, that can be used for signal interception, have been taken into consideration for use with the Grande data acquisition systems and will be discussed in the following sections.

5.2.1 A "current mirror" approach

Provided that the signal source and sink are equipped with low impedance stages, the signal interception can be accomplished by mirroring the current [2] into the original DAQ system's input to the inputs of additional data acquisition systems.

An indispensable prerequisite for successfully distributing signals this way is a highly linear circuit providing high fidelity with respect to distortions and frequency response. The basic idea of a simple current mirror circuit is shown in figure 5.1. That type of current mirror device is lacking any kind of temperature compensation though. In order to achieve proper operation (implying high linearity and current balance), it is vital that the transistors are matched with respect to all parameters, i.e. only selected parts should be used to assemble that kind of circuit.

The Widlar current mirror circuit is a more sophisticated type of device. Its schematic is shown in figure 5.2. In comparison to the simple type of current mirror device mentioned above, the Widlar type of device is enhanced with regard to thermal stability. Nevertheless, the components of this circuit have to be selected carefully as well for maximum performance and there must not be a difference in temperature for the parts from which the current mirror is built, i.e. there should be no temperature gradient whatsoever.

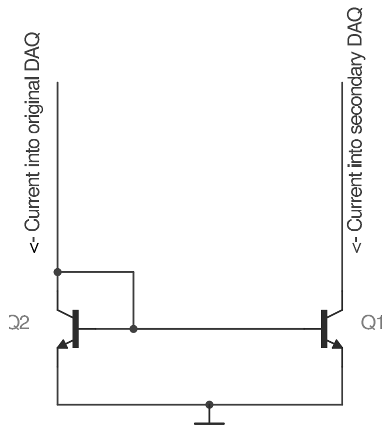

Figure 5.1: Schematics of a simple type of current mirror.

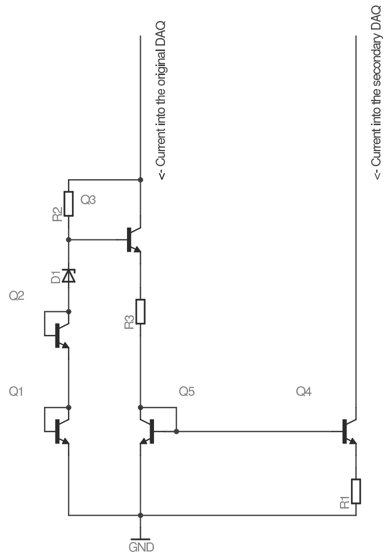

Figure 5.2: Schematics of the Widlar current mirror.

The current mirror approaches above are only mentioned in order to explain the concept of current mirroring. Those devices do not work at all for voltages far below the turn-on voltage of the transistors or for AC signals.

For applications, where galvanic insulation as well as the transmission of analog current signals via optical fibers are most essential, a circuit architecture called “OCCM” [3] may be the best solution. It can prove useful in situations, where high voltages or potential problems concerning ground loops require the current mirror device to be separated galvanically.

5.2.2 The “active probe” method

Besides the methods described in 5.2.1, there is another way for signal interception. A device with a high impedance input stage may be connected to the signal source directly, thereby leaving the original connection nearly unchanged avoiding a branch line which would cause interferences otherwise. A device similar to that shown in figure 5.3 may be used. Provided that the operational amplifier is capable of processing the source signal with high signal fidelity and the additional load caused by it is far below that of the original source by several orders of magnitude, the impact of this type of circuit on the signal transmission is negligible. If the additional complex load would reach the same order of magnitude like the original DAQ system, the signal power would partially be diverted into the intercepting device.

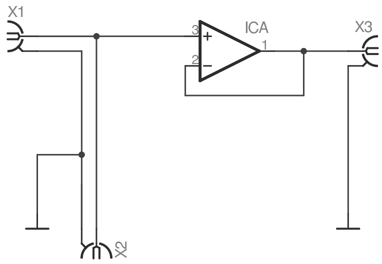

Figure 5.3: Block schematic of the active probe device.

The active probe devices used for the Grande array stations fulfill all criteria and do not show any impact on the original signals. See appendix D for additional information on the implementation of the active probe device.

5.3 Methods for splitting a signal

Another solution for the parallel operation of data acquisition systems is to install an active splitting device, i.e. a device which distributes a source signal to some destination devices, which in turn form the input units of the systems. This method keeps the systems independent of each other, not influencing each other's data taking by decoupling them.

5.3.1 A multi-stage solution

One solution to accomplish the signal splitting is the use of a multi-stage amplifier setup as shown in figure 5.4. Due to the fact that multiple amplifier stages are decoupling

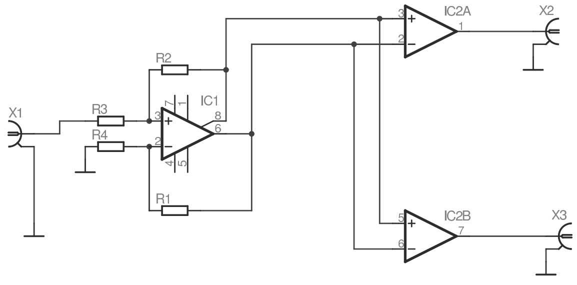

Figure 5.4: Block schematic of a multi-stage splitting device.

the output loads from the signal source, the suppression factor regarding the parasitic feedback of that setup is given by the product of the suppression factors of all the stages. Thus, the source signal remains nearly undistorted in spite of any impact of the DAQ systems on their respective input signals.

There is, however, a drawback involved in using multiple amplifier stages. The noise introduced by e.g. the first amplifier stage is processed by subsequent stages connected to its outputs. As a consequence, the signal to noise ratio diminishes the same way as the feedback suppression increases. The phase shifts vs. frequency of the individual stages add up, whereas the gains of the stages multiply to yield the total gain as a function of the frequency.

5.3.2 The single-stage version

This version of a splitting device is similar to the multi-stage solution above, only the number of stages is reduced to one (see figure 5.5). The disadvantage of directly feeding all the driver stages with the same source signal is negligible, since there are operational amplifiers available, which do not put much load on the signal source for low impedance sources.

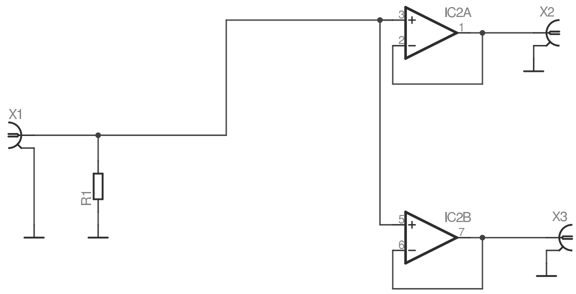

Figure 5.5: Block schematic of a single-stage splitting device.

5.3.3 Comparison of the performance data

A SPICE[1][4] model of a two-stage active splitting unit has been developed in order to compare the performance data of such devices depending on the number of stages actually used. The frequency response regarding both the phase shift and the amplification factor is investigated (see figure 5.6). The transfer function of the entire splitting device results from the convolution of the transfer functions of the particular stages. The frequency response evaluated during the simulation complies with the expectations from the theory. As a matter of fact, the frequency cut-off for the two-stage circuit is lower than for each stage separately, while the phase shift adds up for the entire circuit compared to each single stage.

However, the SPICE models[2] used for modeling the two-stage splitting unit are not including support for the simulation of internal noise nor do they allow the estimation

---

[1] The LTSpice variant by Linear Technology has been used for the simulation.

[2] Analog Devices AD8130 and AD8138

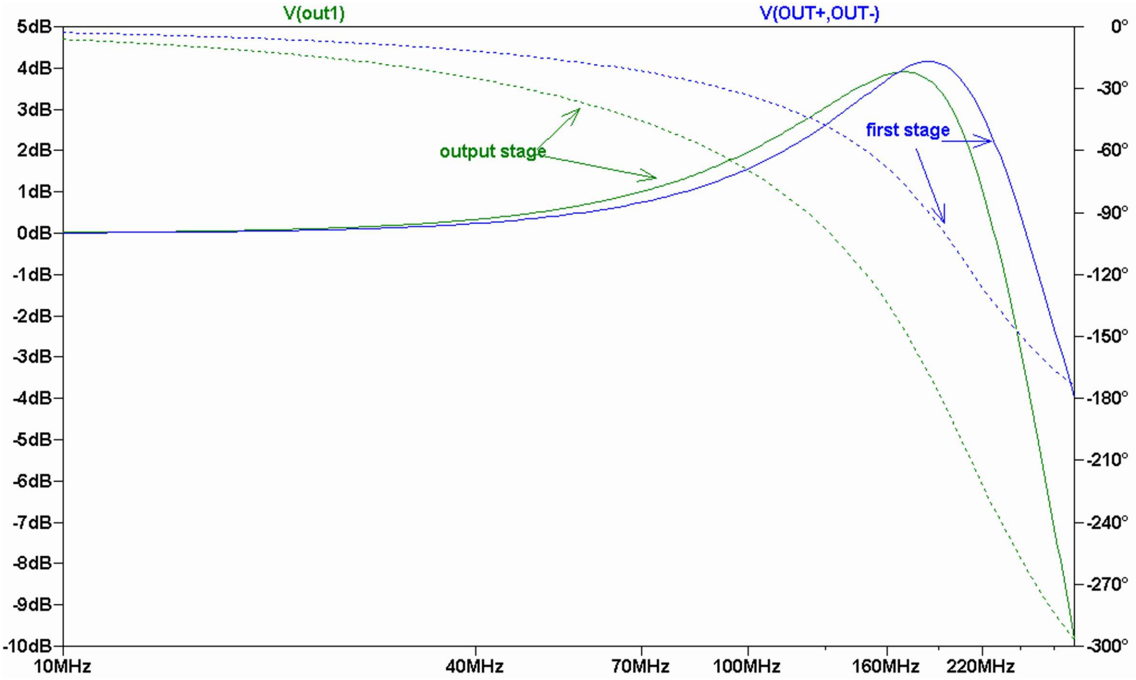

Figure 5.6: Frequency response of a two-stage splitting unit; signals are evaluated for the output stage as well as for the differential outputs of the first stage. Dashed lines indicate the phase shift as a function of frequency, whereas solid lines indicate the amplitudes vs. frequency.

of parasitic feedback effects [28, 29]. Hence, the frequency response vs. the number of stages of the splitting unit can only serve as a hint for the dependency of the feedback suppression and noise vs. the number of stages of the device in question.

5.3.4 Design of a splitting solution based on the results

In order to obtain a splitting device, which offers high signal fidelity, a single-stage solution should be considered the optimum, provided that the amplifier type to be used properly insulates input from output signals. See appendix B for an example of an implementation of the single-stage splitting solution using a state-of-the-art operational amplifier.

Chapter 6

Properties of the KGEMD subsystem

The digitizer subsystem KGEMD has a major impact on the data quality of digitized photomultiplier pulses and for this reason, it strongly affects the overall system's data taking performance. Thus, it is vital to obtain information on the characteristics of this part of the FADC-based data acquisition system.

6.1 The internal structure of the digitizer subsystem KGEMD

A schematic block diagram of the digitizer subsystem KGEMD is presented in figure 6.9. Although the KGEMD is equipped with two digitizer channels, both sampling the pulse waveforms 250 million times per second at a resolution of 12 bits, figure 6.9 shows only the high gain channel in full detail. However, the low gain channel is built exactly like the high gain channel, except for the comparator, which only the high gain channel is equipped with.

The sampling rate of 250 million samples per second and channel is achieved by operating FADCs in a time-interleaved fashion; i.e. several converters are fed with the same signal at the same time and the individual FADC conversions are initiated by phase-shifted clock signals. These constant time skews result in conversions at successive times; thereby, high speed sampling can be achieved using relatively low-cost FADC devices. In the case of the KGEMD digitizer, a 4-fold time-interleaved conversion mode has been chosen, requiring four FADC devices per channel and a conversion rate of 62.5 MHz per each single FADC converter, resulting in a total conversion rate of $4{\times}62.5\,\text{MHz}{=}250\,\text{MHz}$. In order to supply the four FADC devices with the same signal, the KGEMD unit contains a built-in signal splitter, which distributes the source signal to four (in case of the low gain channel) or five (for the high gain channel including the comparator) destinations. A model of the splitting subdevice is described in appendix C.

The FADC devices are continuously digitizing the source signal. Until the comparator encounters a trigger condition (i.e. its threshold is crossed by the source signal), the sampled data is just discarded. Once the trigger condition is fulfilled, the next 252 samples per digitizer channel are sequently buffered within FIFO registers under the control of a FPGA containing some glue logic, i.e. logic, which is needed to coordinate the data flow of the components. With respect to the KGEMD subsystem, the dead time free operation of the FADC-based data acquisition system is caused by the continuous sampling mode and the FIFO registers buffering the data streams. In addition, the FADC converters employed[1] offer an internal output queue, which is used in order to provide pulse shape information up to 48 ns prior to the occurrence of the trigger condition.

For a particular event, the data streams of both the high gain and the low gain channels are multiplexed to form a common data stream, prepended by a sequence of "magic" words (identifying the beginning of a data packet) and a unique KGEMD board number; three time stamp counter values, which are stored along with the sampled data of a particular event, are appended to the data packets. Error detection and correction information [19] constitute the end of the data packets. These packets are then converted into bit-serial data streams in order to be transmitted to the central DAQ station by means of an optical high speed link.

6.2 Impact of the KGEMD temperature dependency on baseline stability

Figure 6.1(a) results from a temperature step analysis of the SPICE model presented in appendix C. The circuit simulator has been used to evaluate the operation point of the KGEMD input circuitry for temperatures ranging from -40 °C up to 80 °C in steps of 5 °C. Considering the temperature range covered inside the KGEMD box during a typical daily cycle as recorded in figure 6.1(b), the baseline deviation caused by the dependency on temperature of the KGEMD subsystem is negligible, since it does not exceed the resolution of the FADC devices attached to the differential outputs (FADC*n*+ and FADC*n*-, where n is a number from 1 to 4). The FADCs, being 12 bit wide flash analogue-to-digital converters configured for a 1 V input voltage range, reach a resolution in terms of the input voltage of 250 μV.

Therefore, the main baseline variation is probably caused by the temperature dependency of the quiescent current of the photomultiplier tubes as well as the high voltage supply's dependency on temperature. However, the temperature behaviour of the FADC devices has not been taken into account in the simulation of the KGEMD input circuitry. There is no manufacturer supplied SPICE model available for the type of device, which the KGEMD has been equipped with. Instead, the manufacturer has supplied an IBIS model, i.e. a behavioural model, which contains the description of the output patterns in response to input signal patterns applied to the particular device. Thus, an IBIS model does not reveal internals of the device in contrast to a SPICE model. It has not been possible to convert the FADC's IBIS model to a SPICE model. As a consequence, the results from the temperature sweep simulation can at best serve as a best-case estimate for the temperature dependency of the circuitry.

---

[1] Analog Devices AD9238

[2] Meilhaus "ZauberDisk" temperature loggers had been used for the measurements.

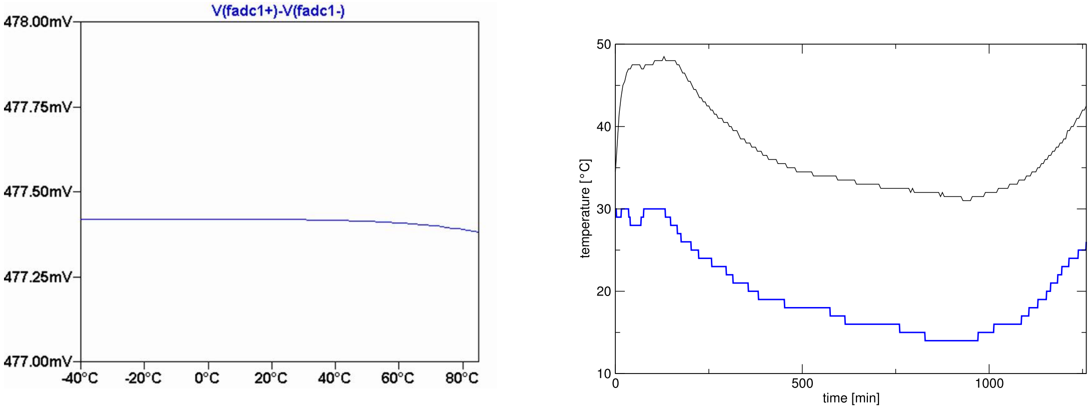

(a) (b)

Figure 6.1: KGEMD baseline variation vs. temperature. (a) The temperature dependence of the baseline voltage has been evaluated by performing a temperature sweep ranging from -40 °C up to +85 °C in steps of 5 °C on the model of the KGEMD input circuitry (see appendix C for more information). The baseline has been evaluated as the differential signal of the FADC1+ and its FADC1- counterpart. The stages, feeding the remaining three FADC converter with the input signal for 4-fold time-interleaved conversion, are built identically; thus, the results evaluated for the first stage are valid for the other stages as well. (b) The development of temperature vs. time is shown, covering a period of 21 hours and starting at 4 o'clock pm, recorded mid-August 2005. The upper curve has been taken inside the KGEMD box (enclosing the actual KGEMD unit), whereas the lower curve shows the environmental temperature of the KGEMD box, i.e. it has been recorded inside the same Grande array station [19]. The error of the temperature measurements performed by autonomous data loggers[2]amounts to ±1 °C.

6.3 Frequency response of the KGEMD input circuitry

The frequency response behaviour of the KGEMD input circuitry is illustrated in figure 6.3. The response is depending on the environmental temperature, which the input circuitry is exposed to. A frequency sweep simulation has been performed on the model of the circuitry and the simulation runs have been repeated for temperatures ranging from −40 °C up to +85 °C in steps of 5 °C. The frequency range covered during the simulation runs has been limited to 125 MHz, corresponding to the Nyquist frequency of the digitizer subsystem. For the temperatures to be expected inside the KGEMD boxes (according to 6.1(b)), the splitting section of the KGEMD input circuitry exhibits an amplitude degradation of up to 25% for signal components near the Nyquist limit.

Bandwidth limitations can be illustrated by means of a square wave stimulus signal as well. The sharp trailing and falling edges of square waves result in spectral contributions at high frequencies. Bandwidth limitations cause overshoot distortions (often referred to as "edge ringing") for sharp-edged signals; this effect is called the *Gibbs phenomenon*. The KGEMD input circuitry responds to an excitation by a square wave signal with overshoot contributions (see figure 6.3).

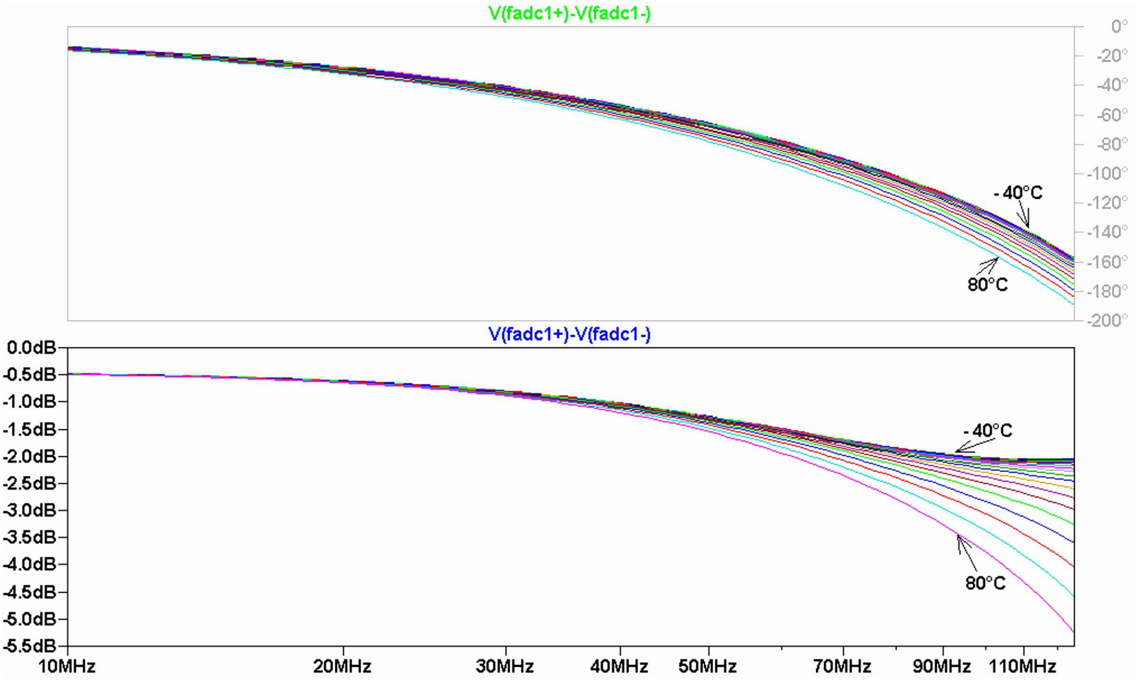

Figure 6.2: Frequency response of the KGEMD input circuitry vs. temperature. For clarity, the group phase shifts and the corresponding amplitudes have been drawn in different panes; they have been plotted as a function of frequency and share the same horizontal axis. The frequency range has been limited to the Nyquist frequency of the FADC devices onboard the KGEMD unit; the frequency range below 10 MHz has been omitted for enhanced visibility in the high frequency area, since the response can be considered flat for lower frequencies down to 0 Hz due to the DC coupling of the KGEMD input circuitry—see the SPICE model in figure C.1. The phase shift response has been plotted inside the upper pane, whereas the amplitude response is shown within the lower pane. The temperature value has been swept from -40 °C up to +85 °C in steps of 5 °C during the simulation of the model.

As a consequence, a spectral projection function has been constructed, similar to that, which has been used in chapter 3 in order to compensate for the shaping amplifier's impact on its input signal. Here, an inverse quadratic fit has been applied to the amplitude as a function of the frequency (see figure 6.3).

$$p(f) = (a_0 + a_1 f + a_2 f^2)^{-1} \tag{6.1}$$

The following parameters have been calculated by the regression algorithm.

$$\begin{aligned} a_0 &= 0.99092, \\ a_1 &= 2.1092 \cdot 10^{-9}\mathrm{s}, \\ a_2 &= 5.1634 \cdot 10^{-19}\mathrm{s}^2. \end{aligned}$$

The regression algorithm yielded a standard deviation of $\sigma = 0.02$.

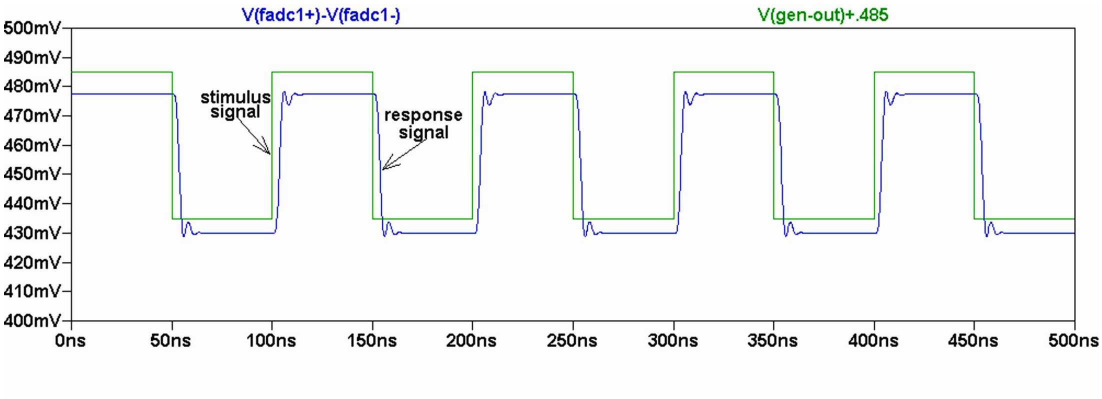

Figure 6.3: Response of the KGEMD input circuitry excited by a square wave signal. The square wave stimulus signal has been shifted vertically in order to allow simultaneous display of both the stimulus and the response. As a consequence of its bandwidth limitations [26], the KGEMD input circuitry responds to the sharp trailing and falling edges of the stimulus (rise and fall times $t_\uparrow \approx t_\downarrow \approx 1$ ps) with overshoot contributions ("edge ringing") at the respective rising and falling edges of the response signal; this is commonly referred to as the Gibbs phenomenon. The time shift of the response signal with regard to the square wave stimulus is due to the circuitry's propagation delay time.

The enhancement, that can be achieved by applying the spectral projection function, is shown in figure 6.4. In order to apply the correction, the square wave signal modified by the KGEMD response has been transformed into the frequency domain using a discrete Fourier transform, the spectral components were then multiplied by the respective results from equation 6.1. The corrected waveform in figure 6.4 has been obtained by converting the spectral data back into the time domain.

The spectral projection function cannot compensate for all deviations; thus, the waveform is still different from the stimulus. Due to the fact, that the fit of the spectral distribution has been limited to the first Nyquist zone (i.e. to frequencies below the Nyquist frequency), equation 6.1 does not coincide with the distribution at highest frequencies. However, the SPICE simulation does not comply with the real hardware devices at these frequencies either.

6.4 Time-interleaved analogue-to-digital conversion

There are mainly three ways of speeding up analogue-to-digital conversions.

- Employment of state-of-the-art ADC devices; in most cases, this is not an option for use in e.g. a large detection array, since these devices are usually too expensive. Furthermore, most of these devices show high power consumption and heat production, which may be harmful in e.g. closed boxes or in environments, where

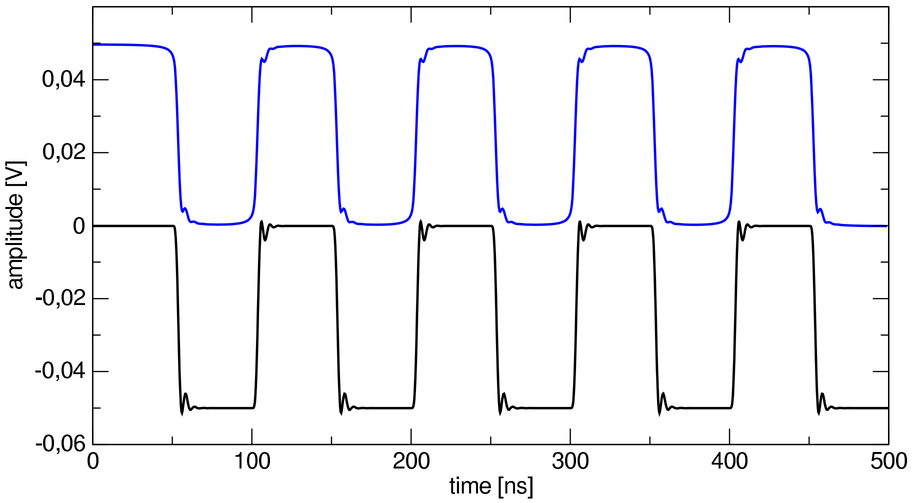

Figure 6.4: KGEMD response to a square wave after response compensation. The waveforms have been shifted vertically for their simultaneous display within one figure. The waveform on the bottom corresponds to the differential output waveform of the KGEMD subsystem's input circuitry (as presented in appendix C) in response to a square wave excitation. The upper waveform shows the results of a frequency response correction of the same setup; here, the output signal has been sampled, was transformed to the frequency domain using a discrete Fourier transform, the frequency response has been corrected by a spectral projection function and, finally, the response in the time domain was evaluated by an inverse DFT. The overshoot could not be compensated completely; the square wave covers a broad spectral range, whereas the spectral projection function aims only at compensating the frequency response within the first Nyquist zone, i.e. up to the Nyquist frequency.

electrical power is strongly limited. The devices usually have not proven their long term stability yet either;

- Operating FADCs in a time-interleaved fashion; this allows the use of relatively low-cost devices for high speed conversions. The KGEMD subsystem uses time-interleaved conversion mode, therefore it is described below in more detail;

- A hybrid filter bank analogue-to-digital (HFB-ADC) architecture [31]; here, the source signal to be digitized is first analyzed using analogue filter banks. Each filter bank allocates a spectral range for one ADC device of an ADC array. Hence, all ADCs are dedicated to sample the source signal with respect to contributions to one frequency band each. For the reconstruction of the digitized source signal, the frequency bands are merged again using digital synthesis filters. This approach allows the employment of low-cost ADC devices; in contrast to the standard time-interleaved array conversion technique, even though it allows the employment of the same type of ADC device, the HFB-ADC architecture offers superior conversion speed and sampling resolution. This improvement over the time-interleaved technique is achieved by attenuating the ADC property mismatches, i.e. different gain values or offset voltages as well as timing errors. Designing hybrid filter banks poses a challenge, though. An adequate channel separation within the analogue analysis filters as well as a proper signal reconstruction by means of the digital synthesis filter is mandatory for the distortionless operation of the HFB-ADC. Maldesigned hybrid filter banks may introduce gain and phase distortions; even aliasing effects may be caused by poorly implemented HFB-ADCs.

6.4.1 The underlying principle of time-interleaved analogue-to-digital conversion

Time-interleaved analogue-to-digital conversion requires:

- A set of identical ADC converters with the same properties (within small tolerances);
- A stable clock source, supplying the ADC converters with phase shifted clock signals;
- Some glue logic, which takes care of data multiplexing.

The ADC devices are supplied with conversion clock signals derived from a master clock. For successive sampling, i.e. to allow time-interleaved operation, a suitable clock delay provides the respective phase shift for each of the ADCs. Thus, the conversion is triggered for one ADC at a time; the clock signal triggers the ADC's sample-and-hold circuit to sample the input signal common to all ADCs. See figure 6.5 for a simplified model of an ADC device.

6.4.2 Drawbacks and caveats

Using ADC converter devices in a time-interleaved fashion has several implications. Mismatches of the ADC branches in terms of gains, offsets and time jitters can severely limit the resolution of the entire system. For e.g. mismatches in gain of about 3%, the effective number of bits is reduced to 5.8 (for a hypothetical system of otherwise unlimited resolution). Time jitter is another source for the loss of precision; for a time skew of 1.25%, the number of effective bits reduces to approximately 6 for signal frequencies near the Nyquist limit [32]. Thus, it is vital for maximum performance of the device to properly calibrate the ADC array.

Although it is possible to increase the sampling frequency to arbitrarily high values in theory, this does not work for a real device. For one part, the time jitter of the conversion clock limits the maximum frequency for interleaved sampling. In addition, the sample-and-hold circuit must be able to process the signal. At high frequencies, this may result in a loss of precision; for the FADCs used on the KGEMD digitizer subsystem, the FADC resolution is reduced by one bit for signal frequencies beyond 100 MHz.

6.5 Influence of the aliasing effect on signal reconstruction

According to the Nyquist-Shannon sampling theorem, the sampling frequency for digitizing an analogue signal must be at least twice as large as the bandwidth of the analogue

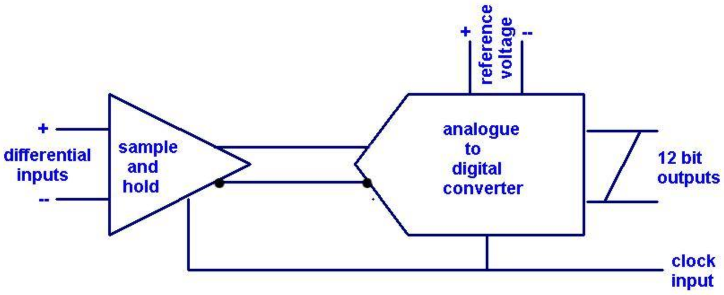

Figure 6.5: Model of an ADC device. Each time a conversion is initiated by a clock signal, the current input signal is sampled by the sample-and-hold circuit and the sampled voltage level is retained as long as the conversion is in progress. After completion of the conversion process inside the ADC core, the result can be accessed at the digital outputs. The conversion of the analogue value is accomplished with regard to the reference voltage. The output value is calculated according to $D_{out} = int((2^N - 1) \times (\frac{U_+ - U_-}{U_{Ref}} + \frac{1}{2}))$, where N denotes the number of ADC output bits, U_+ and U_- indicate the differential ADC inputs and U_{Ref} is the reference voltage.

signal; otherwise the reconstruction of the sampled waveform will not succeed perfectly. If this condition is not fulfilled, i.e. there are spectral contributions of the analogue signal beyond the Nyquist frequency, these contributions are aliased down to the first Nyquist zone. Thus, frequencies beyond the Nyquist frequency are converted into frequencies below the Nyquist limit.

For signals exclusively containing spectral components within one of the Nyquist zones, which are delimited by multiples of the Nyquist frequency, the aliasing effect does not create any problems. The reconstruction algorithm can retrieve the original waveform from the samples despite the aliasing. An example of a sine wave signal with a frequency beyond the Nyquist limit is shown in figure 6.6. The aliasing effect has not been taken into account for the reconstruction; hence, the frequency of the original sine wave is just mapped into the first Nyquist zone.

However, for signals containing spectral contributions of multiple Nyquist zones at the same time, the signal reconstruction will fail because of the ambiguities; it is impossible to retrieve the original signal, since it is not known, whether a specific spectral component is originating from one or the other Nyquist zone. Figure 6.7 illustrates the effect of aliasing for a composition of signals.

By—at least—attenuating contributions from all but one Nyquist zone, the effect of aliasing on the signal reconstruction can be suppressed. This can e.g. be accomplished by inserting an analogue filter (often referred to as an *anti-aliasing filter*) in front of the

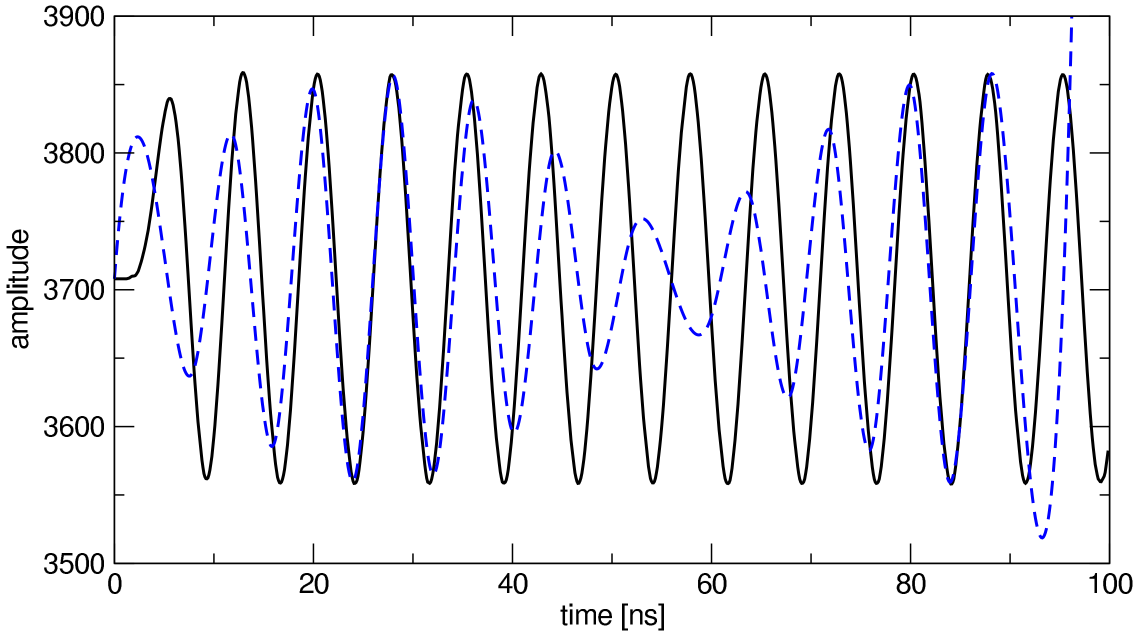

Figure 6.6: Aliasing effect due to sampling beyond the first Nyquist zone. The amplitude axis is subdivided into units of ADC channels. A sine wave to be digitized by the FADC devices is shown (solid line); due to the fact, that the signal is routed through the KGEMD input circuitry, it experiences a drop in the beginning. The frequency of that signal (133MHz) exceeds the Nyquist frequency of the digitizer subsystem KGEMD (125MHz). After digitizing the waveform, the reconstruction of the sine wave results in an interpolated waveform (dashed line), which is aliased down to the first Nyquist zone, i.e. it contains frequencies below the Nyquist limit. High frequency components may therefore be mistaken as low frequency components after sampling and a subsequent waveform reconstruction.

sampling device. However, the filtering cannot be accomplished by means of digital post-processing, since the problem arises already during the sampling itself.

The KGEMD digitizer subsystem does not contain such an anti-aliasing filter; therefore, it is possible to process frequencies beyond the Nyquist limit. On the other hand, the lack of such a filter makes the KGEMD vulnerable to the aliasing effect.

6.6 Effective trigger level vs. PMT pulse duration

One of the branches of the high gain splitting circuitry is feeding the comparator, which defines the trigger condition depending on the preset threshold, with the high gain source signal. In order to allow a fine-grained adjustment of the threshold level, the comparator is not fed with the raw source signal directly; instead, an additional amplifier stage provides the comparator with an increased signal strength. Since the reference voltage (i.e. the threshold) of the comparator is provided by a DAC device offering 12 bit voltage resolution, the amplification is the only way to get over the limited resolution of the threshold setting.

However, according to measurements on the KGEMD subsystem and simulations per-

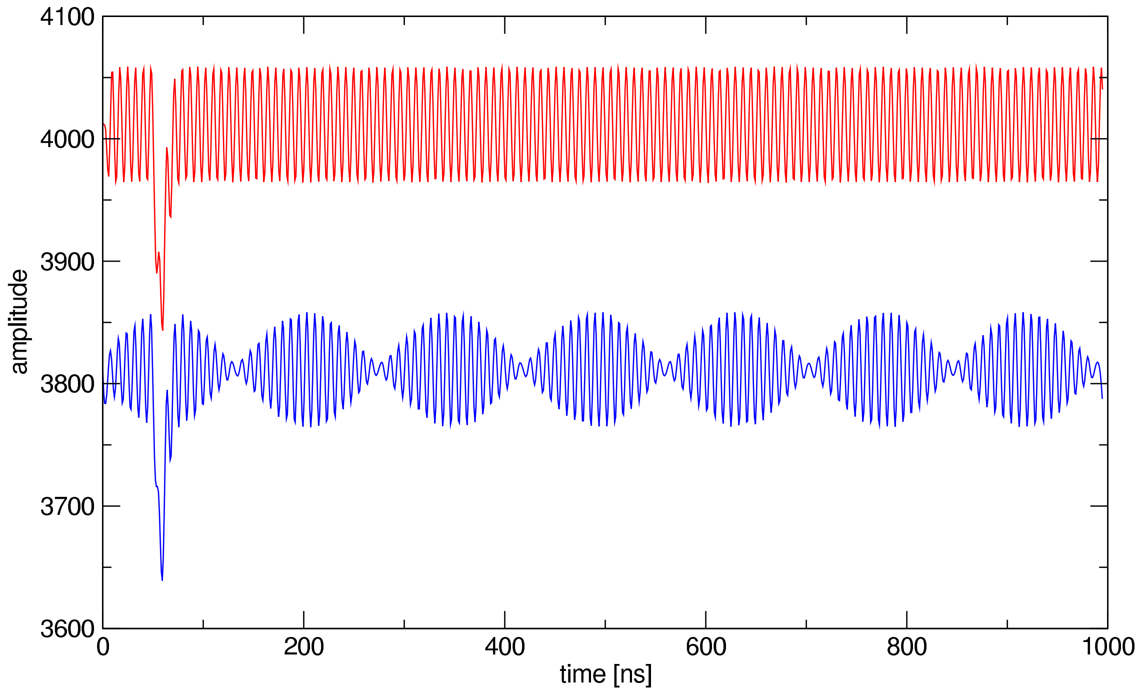

Figure 6.7: Aliasing of an interference signal, that has been added to a simulated single particle pulse. The interference signal's frequency has been chosen to exceed the Nyquist frequency by a few percent; the upper waveform shows the signal prior to the sampling, whereas the lower waveform shows the results of the signal reconstruction. Apart from real interferences, this can serve as an example of the effect of aliasing on high frequency components of a pulse signal.

formed on the SPICE model of the KGEMD subsystem's input circuitry (see appendix C), the additional amplifier stage is highly frequency dependent, i.e. the amplification factor exhibits a drop in the high frequency range. This loss of amplification results in a trigger threshold, which is effectively higher than the value for the low frequency range. The effective trigger threshold vs. the full pulse duration at half maximum (FDHM) is shown in figure 6.8.

Although it would be possible to overcome the constraints of the amplifier stage regarding the signal fidelity by employing another type of amplifier and by differently routing traces on the PCB, the data taking performance of the KGEMD would not benefit from these modifications. The most prominent impact of the response on the trigger system can be observed for m.i.p. pulse signals, since those signals are relatively short with regard to the FDHM. However, by adjusting the comparator threshold of the KGEMD unit accordingly, these pulse signals will nevertheless result in trigger signals. The quality of the waveform sampling is not affected by the limitations of this stage anyway.

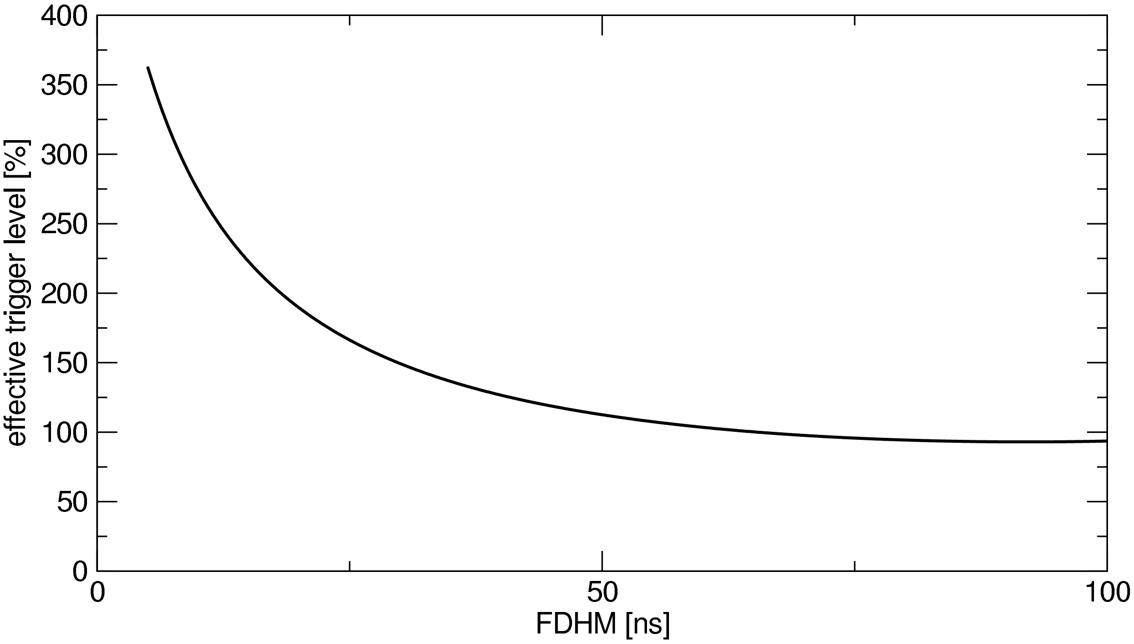

Figure 6.8: Effective trigger level vs. full duration at half maximum (FDHM). The results have been derived from a simulation performed on the model of the KGEMD input circuitry as presented in appendix C; a stimulus of the type described in appendix A has been used to evaluate the dependency. The effective trigger level with respect to the preset threshold voltage has been plotted.

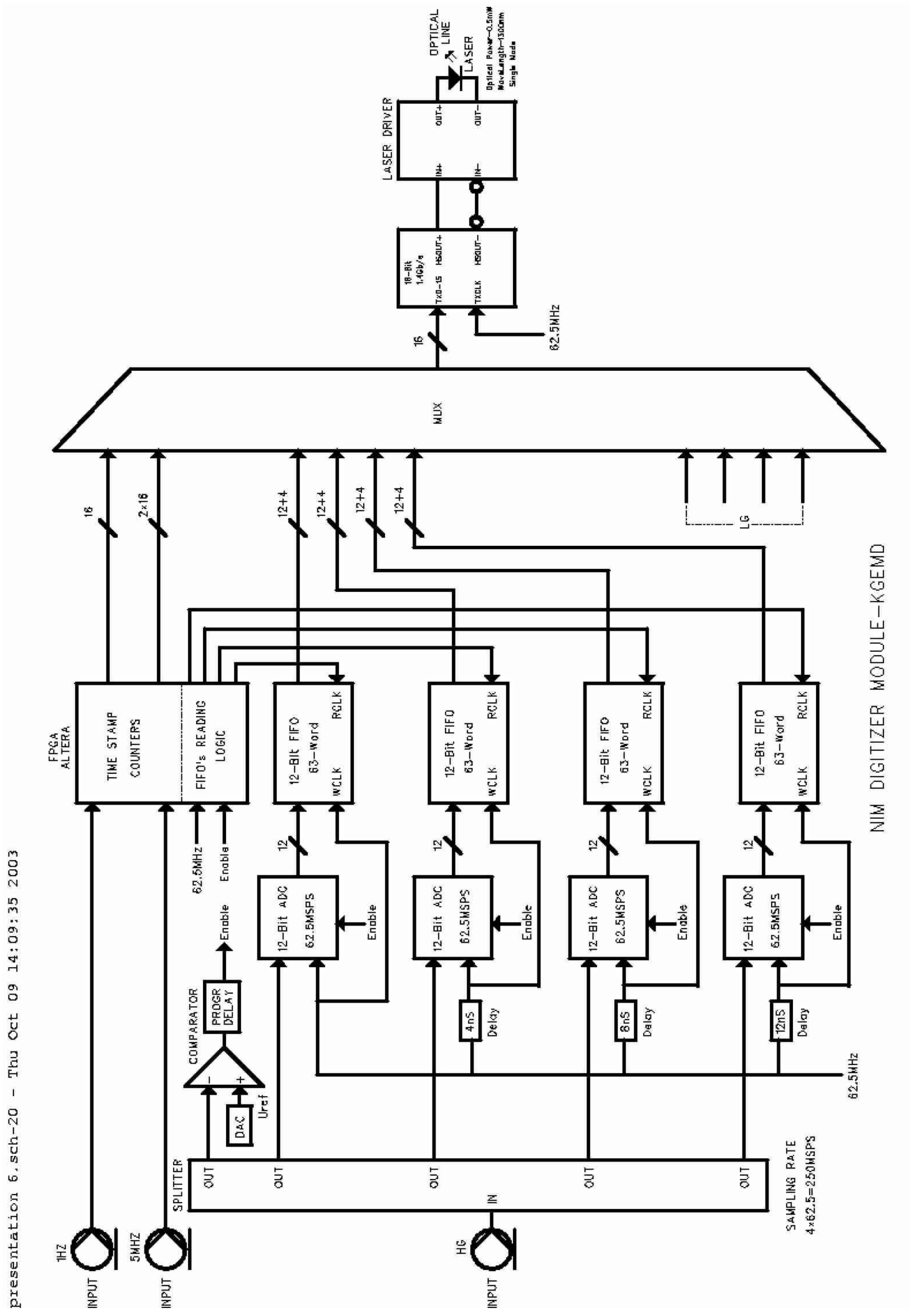

Figure 6.9: Overview diagram of the KGEMD's internal structure [2]; the sketch has been rotated for enhanced visibility. The KGEMD unit is equipped with two channels, which are simultaneously digitizing the mixed signals of the high gain and the low gain photomultipliers, respectively. Only the channel dedicated to the high gain PMTs, is illustrated in more detail; the low gain (LG) channel is only symbolically denoted, since it is built exactly the same way as the high gain (HG) channel, apart from the comparator and its surrounding parts. The KGEMD is receiving time stamp signals from the main KASCADE time base via optical links. Another optical link, operated at a raw data rate of 1.2 Gbit/s (corresponding to 1 Gbit/s for the payload data rate), is established for the transmission of data packets containing—among other things—time stamp information and multiplexed samples of both the high gain and the low gain channel. The data transmission is initiated, if the comparator, which is fed with the high gain signal, encounters a trigger condition, which requires, that the high gain photomultiplier source signal is crossing the threshold level of the comparator.

Chapter 7

Summary and outlook

In July 2005, the installation of the new FADC-based data acquisition system in the Grande array of the KASCADE-Grande experiment has been finished. The DAQ system has been commissioned concurrently to the original Grande DAQ system, which it outperforms in many respects.

The measures taken in order to operate the FADC-based system in parallel, have been described within this thesis. Since it is only possible to reach the full potential of a high performance data acquisition system, which is capable of supplying pulse shape information at a high resolution in addition to the energy spectra and arrival times, if detailed information on the system constraints as well as on the interactions of both DAQ systems are available, these items have been examined as a part of this thesis.

Although the new FADC-based system meets most of its design goals, others require means of compensation in order to achieve optimal performance data. Some of the methods for compensation are already covered by this thesis, other issues may have to be worked on in future. For example, automatic intercalibration has not yet been implemented completely. Sophisticated methods of digital signal processing, e.g. noise suppression or digital filtering, have not been developed yet. These items will require additional research and efforts.

However, the full pulse shape data of extensive air shower events, which trigger the central event builder, is recorded and kept. Thus, these means of data post-processing can be applied to the resulting data files, once the respective algorithms have been developed.

On the other hand, the interaction of both data acquisition systems can create problems. Within the scope of this thesis, the effects on the data taking by the FADC-based system have been estimated. Furthermore, methods for partly compensating for these impacts have been developed.

The FADC-based data acquisition system will be further improved and additional functionality will be implemented. The capabilities and the flexibility of the FADC-based data acquisition system have not yet been exploited entirely. The data taking during the next few years will provide valuable shower data of events in the high energy range covered by the Grande array.

Appendix A

Synthesis of PMT pulse stimuli

In order to conduct some of the SPICE simulations of this thesis, a stimulus had to be created with a pulse shape similar to that of photomultiplier pulses caused by the incidence of a single particle.

While the Landau distribution can, in general, be considered a rough estimate of the real signal shape for simulations, it is, in most cases, not suitable for a SPICE simulation. Usually, the software engine of a SPICE simulator is not capable of evaluating arbitrary mathematical expressions in order to provide a stimulus signal. Moreover, evaluating a complex expression is time consuming and the result of the expression has to be calculated for every simulation step. For a—in terms of the time resolution—fine-grained analysis, the evaluation of the stimulus expression will already consume too much time.

With the SPICE simulator used for the simulations of this thesis[1], it is not possible to use arbitrary functions as a stimulus. However, it is possible to select a damped sine wave as the stimulus. By choosing the parameters accordingly, photomultiplier pulses can be emulated to some extent. The equation has the following form:

$$U_{stim}(t) = -Ae^{-(t-t_0)\lambda} sin(2\pi f(t-t_0)). \tag{A.1}$$

Here, the amplitude can be adjusted by the A parameter, while the pulse duration and the shape of the tail are determined by f and λ. The peak position is controlled by the t_0 parameter. The reason for applying stimuli signals similar to the real waveforms, is, among other things, the spectral composition, which plays an important role for classifying the response behaviour of devices under simulation.

Figure A.1 illustrates the dependency of the amplitude on time for a typical damped sine wave stimulus. For comparison, a Landau distribution, approximated by the Moyal function [34], has been plotted as well. The function values were evaluated from the following equation for appropriately chosen parameters λ_{Moyal} and A_{Moyal}:

$$U_{Moyal}(t) = -A_{Moyal}\sqrt{\frac{exp(-\lambda_{Moyal}(t-t_0) - exp(-\lambda_{Moyal}(t-t_0)))}{2\pi}}. \tag{A.2}$$

In some cases, the sharp kink at the beginning of the damped sine wave stimulus can cause problems, since the first derivative of the stimulus exhibits a discontinuity here, resulting e.g. in high frequency contributions to the respective spectrum.

---

[1] LTSpice by Linear Technology

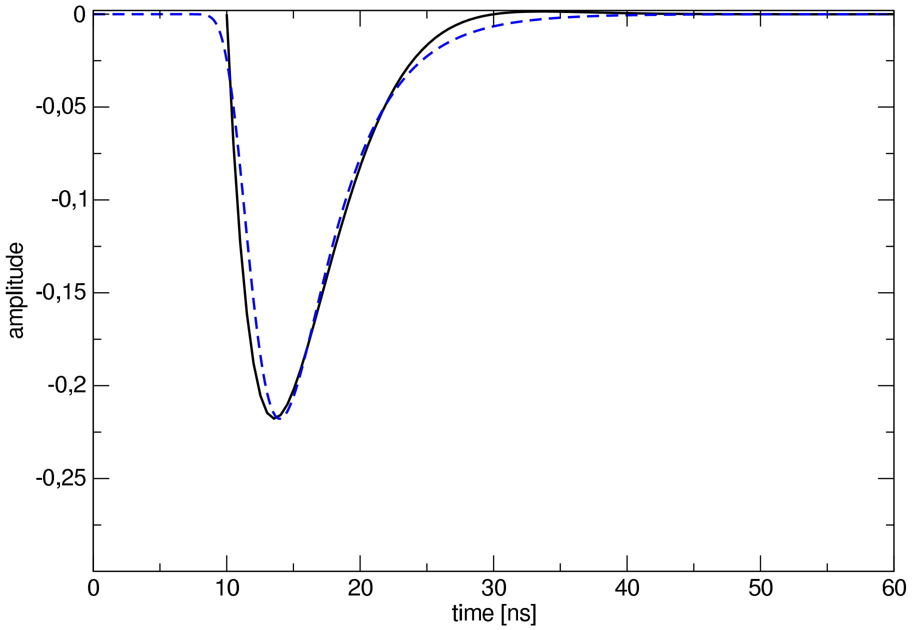

Figure A.1: Typical damped sine wave stimulus (solid line). The Moyal approximation of the Landau distribution is plotted for illustration (dashed line).

Appendix B

Example of a splitting device

An example of a splitting circuit has been developed as a consequence of the results from chapter 5. A draft of the schematic diagram is shown in figure B.1.

The operational amplifier[1] selected is a state-of-the-art type [22]. It offers low noise ($0.95\,\mathrm{nV}/\sqrt{\mathrm{Hz}}$) and low distortion at high speed ratings. Its input impedance is about five orders of magnitude higher than that of a standard $50\,\Omega$ signal source. Thus, this single-stage splitter should only put a negligible amount of load to the source.

The operational amplifier employed exhibits unstable behaviour for an unity gain configuration; therefore, it has been configured for an amplification by a factor of two and the voltage levels are corrected by means of serial resistors, which provide the impedance matching at the same time. Furthermore, the operational amplifier used in the schematic is sensitive to complex loads, which are attached to the output directly, e.g. a transmission line. The serial resistors provide decoupling from the complex component of the signal sink, thereby minimizing the problem.

The frequency response of the splitting device has been evaluated for one splitter channel using a SPICE model of the device. The -3 dB bandwidth of the device can be gathered from figure B.2; it can be estimated to 568 MHz.

A splitting device should provide highly symmetric output signals to both signal sinks, i.e. the differential signal should be vanishingly small. From figure B.3, it can be verified, that this prerequisite is fulfilled.

Because of the overall properties of the device, this example of a versatile splitting device will suffice for many splitting tasks, where the bandwidth meets the requirements. This makes it e.g. suitable for the frequency range covered by the digitizer subsystem KGEMD.

---

[1] AD8099 by Analog Devices [33]

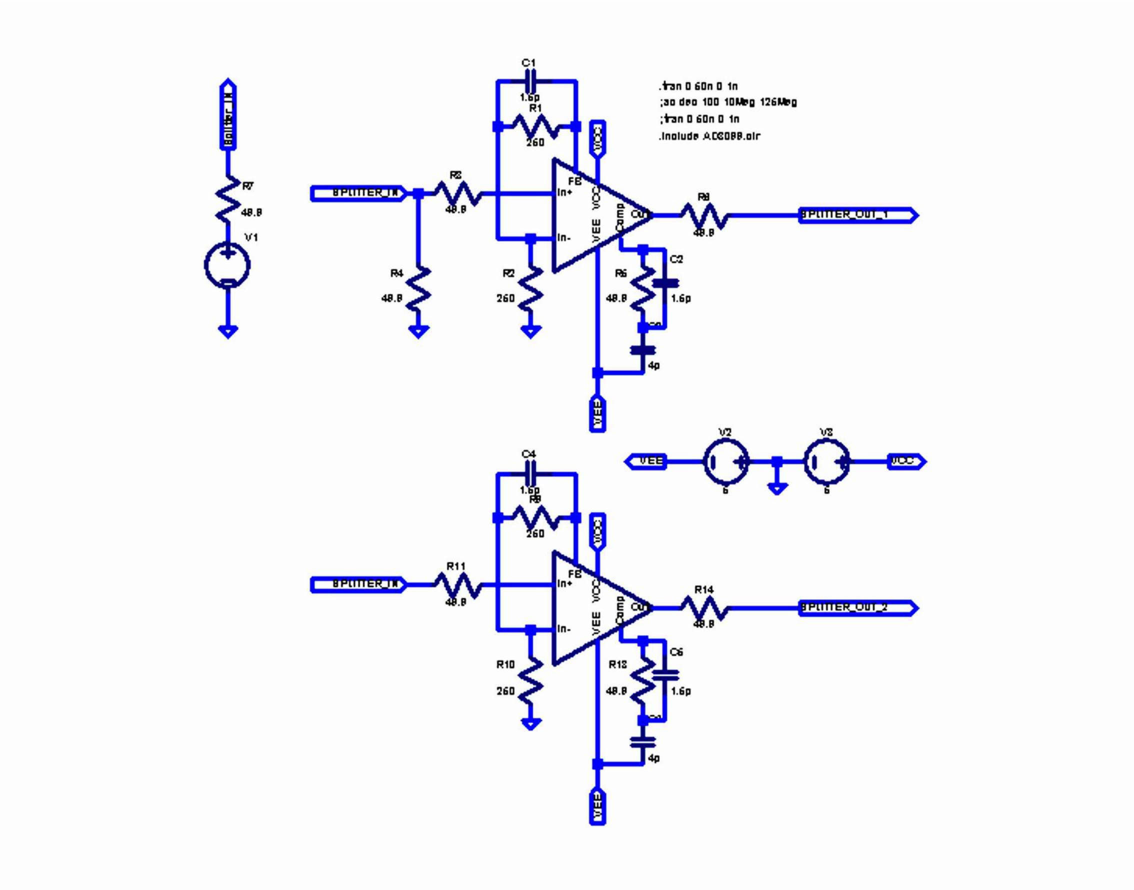

Figure B.1: Example of a splitting device. Input and output terminals of the device are terminated using 50 Ω resistors; coaxial cables matching this impedance can therefore be connected directly. Since the operational amplifier is not stable for unity gain, it has been configured for an amplification factor of two and the output voltage is divided again by the same factor using a serial resistor, which at the same time provides the impedance matching for the output terminals.

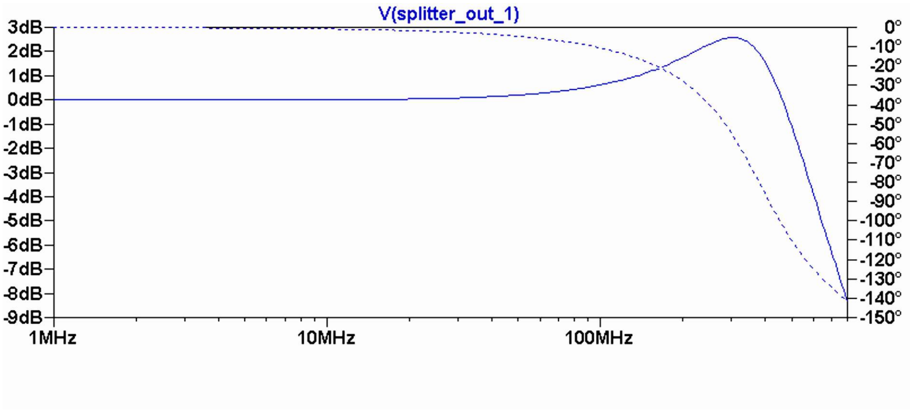

Figure B.2: Response of the splitting device vs. frequency. The response has been evaluated using a SPICE model of the device. The phase shift is depicted by a dashed line, whereas the magnitude is drawn as a solid line. Only the response of one splitter channel has been plotted, because the circuit is symmetrical with respect to the amplifier stages. From the frequency sweep run, the -3 dB bandwidth can be estimated to 568 MHz.

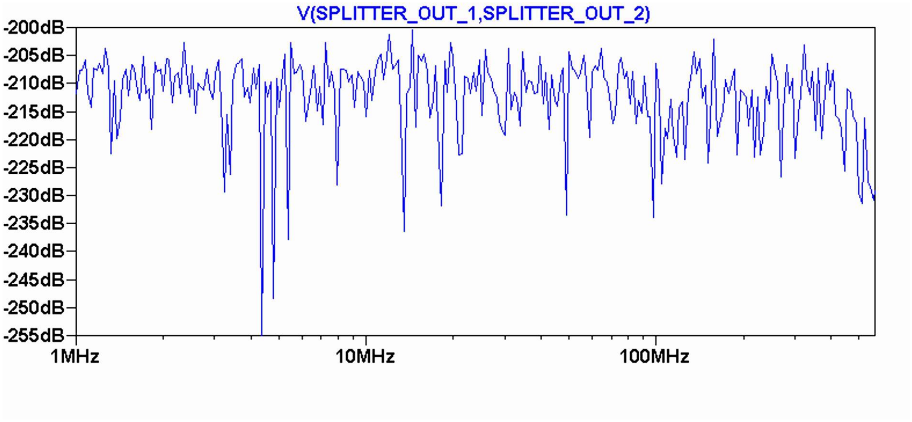

Figure B.3: Deviation of the splitted signals from one another vs. frequency. The deviation has been calculated as the differential signal of both output signals. The simulation indicates, that highly symmetric splitting is achieved by the splitting device over the whole range up to the -3 dB bandwidth.

Appendix C

SPICE model of the KGEMD input circuitry

The SPICE [4] model shown in figure C.1 has been derived from the schematic diagram of the digitizer subsystem (KGEMD) [2]. All components, which do not affect the dynamic characteristics of the KGEMD input circuitry, have been replaced by less complex elements (partly objects intrinsic to the SPICE software[1]) or have even been removed completely without substitutes, for simplicity. An example of the latter category are the power supply bypassing components, which have been omitted, because the power supply wiring is lossless by definition in SPICE simulations, i.e. there is no need for bypassing measures. On the other hand, e.g. voltage references for shifting the input voltage range or adjusting the operation point of the amplifier stages in figure C.1 are mandatory for the proper operation of the circuitry; however, it does not matter, exactly how the voltage reference circuit is working internally. Therefore, the voltage reference sub-circuits have been replaced by standard SPICE DC voltage source objects.

By reducing the number of components involved in the simulation, the number of wiring nodes decreases. Taking into account, that the SPICE models of operational amplifiers [29, 28], used to assemble the KGEMD input circuitry model, are rather complex, i.e. they use up a considerable amount of wiring nodes internally [29, 28], the limits of the respective simulation engine may be exceeded easily. Since the voltages and currents of each single wiring node of a SPICE model must be evaluated by means of numerical computing for every simulation time step throughout the complete simulation run, it is advisable to keep the number of wiring nodes as low as possible. In rare cases, the numerical computation procedure—the Newton-Raphson iteration method is used as of version 3 of Berkeley SPICE—may even fail to converge for models containing too many wiring nodes. The main reason for keeping the number of wiring nodes low, is, however, the duration of the simulation for a fine-grained analysis in terms of the time step resolution.

---

[1] The LTSpice variant by Linear Technology has been used for the simulation.

C.1 Limitations of the SPICE model

Although the KGEMD input circuitry has been modeled to match the real device as closely as possible, the accuracy of the simulation is limited by several factors. First, the models of the amplifier sub-circuits [29, 28] do not perform simulations of all properties; for example, there is no simulation counterpart for the following properties of the real components:

- inherent noise, i.e. noise that is originating from the device itself, even though the device may be in a quiescent state otherwise;
- distortion effects caused by non-linearities;
- common-mode rejection ratio (CMRR); for an ideal differential amplifier, the output voltage should equal zero, in case, the differential input voltage equals zero, i.e. the input levels are equal. However, for a real device, the output voltage is slightly depending on the absolute input levels; the CMRR indicates the suppression of the effect.

In addition, actually only the properties of simulated components and sub-circuits comprising the KGEMD input circuitry as well as their interconnections are simulated using SPICE. However, for a real setup, i.e. real hardware components, there are additional issues, that have to be considered for optimal performance. These include:

- PCB layout constraints; depending on trace routing, copper area arrangement and component placement, parasitic capacities and inductivities are introduced, which are not covered by the simulation. Moreover, real copper traces exhibit non-zero resistance, which usually does not comply with the properties of the wiring in a SPICE simulation;
- interferences caused by surrounding circuitry; in general, the circuitry to be analyzed using SPICE modeling techniques, is treated as an insulated device, i.e. a device, which is not exposed to interfering signals caused by adjacent sources. In contrast, real hardware devices may even malfunction due to interferences;
- non-ideal components; parasitic contributions result in modifications to the overall properties, which are not modeled by basic SPICE components.

Nevertheless, despite these limitations, the SPICE model presented can provide a clue to the overall performance and properties of the KGEMD input circuitry, thereby allowing to estimate its pulse signal fidelity.

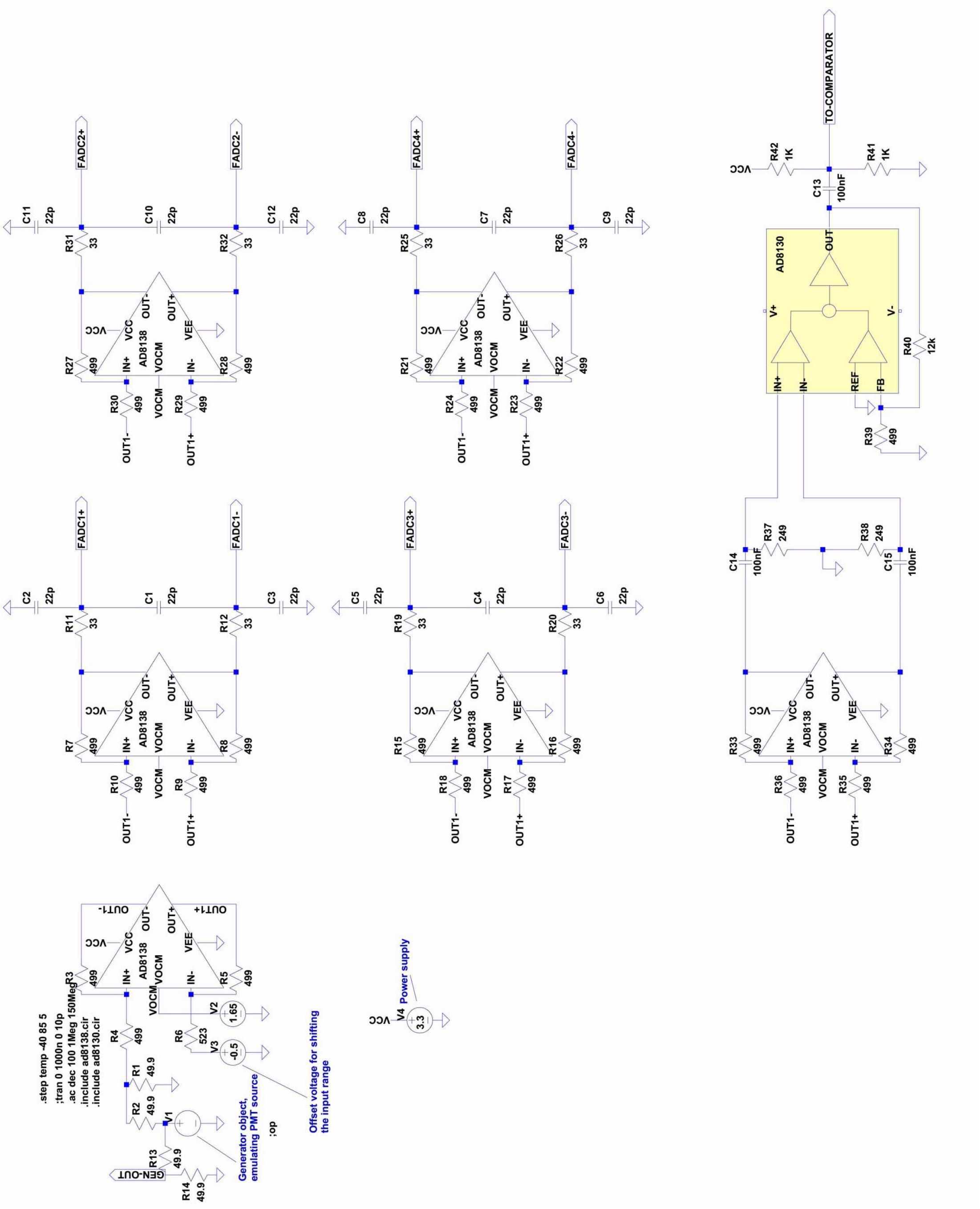

Figure C.1: SPICE model of the KGEMD input circuitry. The drawing has been rotated for enhanced readability. Only the high gain input circuitry is shown. Since the low gain part of the KGEMDs is equipped exactly the same way and is only lacking the amplifiers, which feed the trigger comparator, the properties of the high gain circuitry can, however, serve as a worst-case estimation for the low gain channel properties. Therefore, the two amplifiers at the bottom, including surrounding parts, are solely mandatory for high gain channel simulations. Again, the generator object V1 may be used to either emulate PMT pulse signals or feed the circuitry with arbitrary test signals, e.g. for frequency sweep measurements. The terminals denoted as FADC$n+$ and FADC$n-$, respectively, where n is a number from 1 to 4, refer to the differential inputs of the FADCs, which are operated in time-interleaved conversion mode in order to quadruple the effective sampling frequency.

Appendix D

Characteristics of the “Active Probe”

The “Active Probe” device has been developed in order to enable the digitizer subsystem of the new FADC-based DAQ system to intercept mixed PMT signals from the original Grande DAQ system, which is operated concurrently.

The device has been designed with several goals in mind.

- It should only put a marginal amount of extra load on the intercepted signal. The input impedance of the employed amplifier is about 10^5 times higher than the impedance of the signal source. Therefore, the additional load is negligible.
- There should be no extra noise originating from the intercepting device. Since the original signal chain is kept and no active component is introduced in between its components, there is virtually no way to introduce noise contributions into the original signal chain. However, the internal noise of the intercepting device’s active component is added to the signal, that is read and processed by the digitizer component. The operational amplifier[1] used to build the “Active Probe” device offers a low noise factor of $12.5\,\mathrm{nV}/\sqrt{\mathrm{Hz}}$. This helps to minimize the effect.
- In order not to reduce the digitizing accuracy of the KGEMD subsystem by introducing time jitter, it is advisable to employ an operational amplifier, which features an active feedback stage, since the phase accuracy can be improved by means of such a stage [23].
- The frequency response up to (at least) the digitizer’s Nyquist frequency needs to be flat in order to provide high pulse signal fidelity to the KGEMD input signal. By selecting an adequate type of operational amplifier, this can be guaranteed for the “Active Probe” device. In addition, special care has been taken to design the printed circuit board (PCB) of the device according to the manufacturer’s recommendations with respect to trace routing and power bypassing (among other things).
- The device has to be located near the output connector of the signal source and there must not be a branch line connecting the “Active Probe” device to the original signal pathway to be spied on. Otherwise, reflections and interference may occur, which would cause modifications to the original pulse signals. The “Active Probe”

---

[1] Analog Devices AD8130

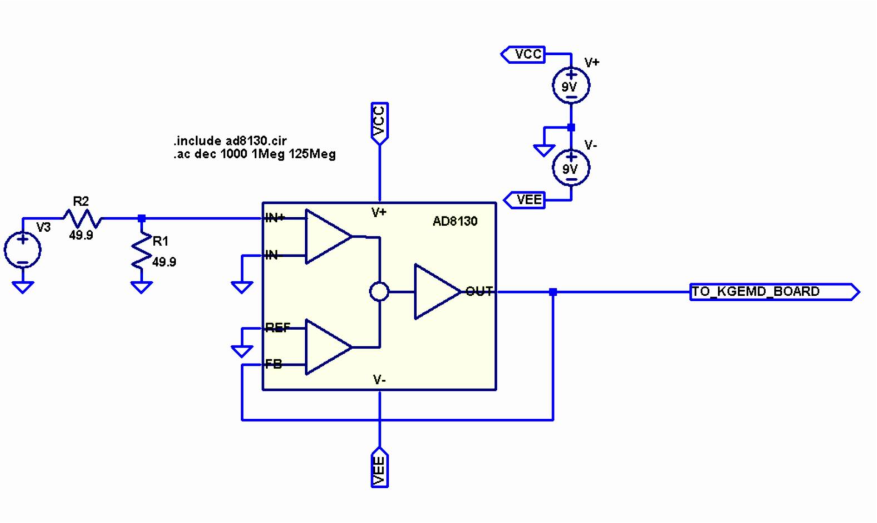

Figure D.1: SPICE model of the “Active Probe” device as deployed in the Grande array of the KASCADE-Grande experiment for intercepting the PMT pulse signals from the original Grande data acquisition system. The central component of the “Active Probe” offers active feedback [23] and is represented by its manufacturer supplied SPICE model [28].

device, that has been developed for deployment with the Grande station equipment, has therefore been designed to be a small card, sized only $20 \times 50\,\mathrm{mm}^2$. Thus, it is possible to attach it directly to the output connector of the signal source.

D.1 Results from a simulation of the “Active Probe”

The frequency response of the device has been evaluated by conducting a frequency sweep analysis on its SPICE model (as shown in figure D.1); that is, the amplitude and phase shift were evaluated while the frequency has been increased gradually up to the Nyquist frequency of the digitizer subsystem KGEMD. The response of the “Active Probe” device is shown in figure D.2; except for a little amplitude rise of 5% near the Nyquist frequency, the response is flat, in agreement with the design goals. The phase shift is merely caused by the propagation delay time of the active component.

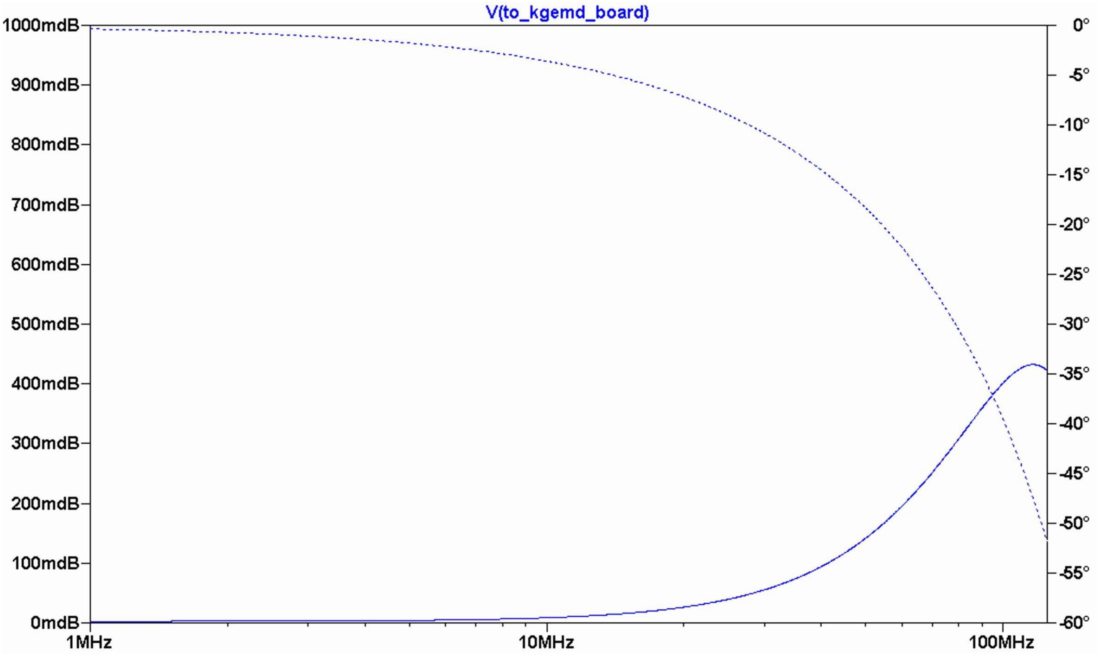

Figure D.2: Dynamic characteristics of the "Active Probe" device. The SPICE simulator has performed a frequency sweep analysis covering the frequency range up to the Nyquist frequency of the FADC-subsystem KGEMD, i.e. up to 125 MHz. The solid line indicates the dependency of the amplification factor on frequency, whereas the phase shift vs. frequency is plotted as a dashed line. According to the results, the "Active Probe" exhibits a maximum deviation of 5% (corresponding to ≈ 0.4 dB) from a flat frequency response.

List of Figures

List of Tables

List of Acronyms

Acronym	Explanation
ADC	Analogue-to-digital converter
CRC	Cyclic redundancy check
DAC	Digital-to-analogue converter
DAQ	Data acquisition (system)
DC	Direct current
DFT	Discrete Fourier transform
DMA	Direct memory access
EAS	Extensive air shower
FADC	Flash analogue-to-digital converter
FDHM	Full duration at half maximum
FFT	Fast Fourier transform
FIFO	First in, first out (register)
FPGA	Field programmable gate array
GPS	Global positioning system
HFB-ADC	Hybrid filter bank analogue-to-digital converter
IBIS	Input/output buffer information specification
KASCADE	Karlsruhe shower core and array detector
KGEMD	KASCADE-Grande electromagnetic detector digitizer board
KGEMP	KASCADE-Grande electromagnetic detector PCI interface card
KGEMS	KASCADE-Grande electromagnetic detector storage board
KGEMT	KASCADE-Grande electromagnetic detector trigger receiver card
LST	Limited streamer tube
LVDS	Low voltage differential signaling
m.i.p.	Minimum ionizing particle
MWPC	Multi-wire proportional chamber
MTD	Muon tracking detector
PC	Personal computer
PCB	Printed circuit board
PCI	Peripheral component interconnect
PMT	Photo multiplier tube
SCSI	Small computer system interface

continued on next page

continued from previous page

Acronym	**Explanation**
SPICE	Simulation program with integrated circuit emphasis
TDC	Time-to-digital converter
VME	Versa module eurocard

Bibliography

[1] S. Over, diploma thesis, *Development and commissioning of data acquisition systems for the KASCADE-Grande experiment*, University of Siegen, 2004

[2] Y. Kolotaev, 2005, private communication.

[3] D. V. Camin et al., *Galvanically isolated and linear transmission of analog current-signals using the optically coupled current-mirror architecture*, Nuclear Instruments and Methods **A535** (2004) 485-490

[4] L. W. Nagel, *SPICE2: A Computer Program to Simulate Semiconductor Circuits*, University of California, Berkeley **ERL-M520** (1975)

[5] P. L. Biermann et al., *Cosmic Rays from PeV to ZeV, Stellar Evolution, Supernova Physics and Gamma Ray Bursts*, preprint astro-ph/0302201

[6] see e.g. references in: C. Grupen, *Astroparticle physics*, Springer-Verlag, Berlin, 2005

[7] J. Zabierowski et al., *Large muon tracking detector in the KASCADE EAS experiment*, Proceedings 27th International Cosmic Ray Conference (ICRC 2001), 810-813

[8] A. Haungs et al., *The KASCADE-Grande experiment*, Proceedings 28th International Cosmic Ray Conference (ICRC 2003), 985-988

[9] M. Müller et al., *A measurement of the energy spectrum of unaccompanied hadrons*, Proceedings 28th International Cosmic Ray Conference (ICRC 2003), 101-104

[10] A. Haungs et al., *Astrophysics of the knee in the cosmic ray energy spectrum*, Acta Physica Polonica B **35** (2004) 331-339

[11] J. Candia et al., *Cosmic ray spectrum and anisotropies from the knee to the second knee*, J. Cosmol. Astropart. Phys. 05, **3** (2003)

[12] M. Nagano and A. A. Watson, *Ultrahigh-energy cosmic rays*, Reviews of Modern Physics **72** (2000) 689-728

[13] S. Eidelman et al., *Review of Particle Physics*, Physics Letters B **592**, 1 (2004)

[14] O. Alkhofer, *Introduction to cosmic radiation*, Verlag Carl Thiemig München, 1975.

[15] T. J. Kutter, *The water cherenkov detector in the Auger experiment*, FZKA-6396

[16] T. Antoni et al. *The cosmic ray experiment KASCADE*, Nuclear Instruments and Methods **A513** (2003) 490-510

[17] M. Aglietta, *The cosmic ray primary composition in the 'knee' region through the EAS electromagnetic and muon measurements at EAS-TOP*, Astroparticle Physics **21** (2004), 583-596

[18] M. Aglietta, *UHE cosmic ray event reconstruction by the electromagnetic detector of EAS-TOP*, Nuclear Instruments and Methods **A336** (1993), 310-321

[19] S. Over, 2005, private communication.

[20] D. Zimmermann, 2005, private communication.

[21] B. Schöfer, 2004, private communication.

[22] R. Seibert, 2005, private communication.

[23] J. Wong, *Active feedback improves amplifier phase accuracy*, Analog Devices Application Notes **AN-107** (1987)

[24] V. Andrei, diploma thesis, *Reconstruction algorithms for the FADC DAQ system of the KASCADE-Grande experiment*, University of Siegen, 2004

[25] M. Frigo and S. Johnson, *The design and implementation of FFTW3*, Proceedings of the IEEE **93** (2005) 216-231

[26] J. Pickerd, *DSP in high performance oscilloscopes*, Tektronix Inc., 2005

[27] *Product specification XP3462*, Photonis, 1999

[28] *Differential receiver amplifiers AD8129/AD8130, data sheet and SPICE model*, Analog Devices, Rev. A

[29] *Low distortion differential ADC driver AD8138, data sheet and SPICE model*, Analog Devices, Rev. E

[30] J. Bird, *Detection of a cosmic ray with measured energy well beyond the expected spectral cutoff due to cosmic microwave radiation*, preprint astro-ph/9410067

[31] S. Velazquez, T. Nguyen and S. Broadstone, *Design of hybrid filter banks for analog/digital conversion*, IEEE Trans. Signal Processing **46** (1998) 956-967

[32] A. Montijo, *Accuracy in interleaved ADC systems*, Hewlett-Packard Journal, 1993.

[33] *Ultralow distortion, high speed 0.95 nV/$\sqrt{Hz}$ voltage noise Op Amp*, Analog Devices, Rev. B

[34] J. Moyal, *Theory of ionization fluctuations*, Phil. Mag. **46** (1955)

Acknowledgement

My gratitude goes out to all those, who made this thesis possible.

In the first place, this is without doubt Prof. Dr. Peter Buchholz, who made it possible for me to work on the interesting KASCADE-Grande experiment. Furthermore, I would like to thank him for the opportunity to take part in the research within the scope of another exciting experiment in the future.

I am also very grateful that Prof. Dr. Claus Grupen agreed to revise this thesis—despite the brevity of the time available.

I can hardly thank all the people of our working group adequately for the pleasant atmosphere. It made working on the experiment and the thesis a lot easier. Very special thanks to my colleagues who worked on the KASCADE-Grande experiment as well, since they were all able and willing to work as a team.

Also, I am indebted to Marc Brüggemann, Sven Over and Dirk Zimmermann, not only for patiently proofreading the contents of my thesis but also for sharing my sense of humour, irony and even sarcasm. This led to a lot of funny discussions e.g. during lunch.

Thanks to Dr. Wolfgang Walkowiak for the hints on—among other things—formal aspects of my thesis.

In addition, I would like to thank Yury Kolotaev and Bernd Schöfer for their design work regarding the KASCADE-Grande experiment and I'd like to extend my thanks to the members of the mechanical and the electronics workshops, who contributed to building the setup of the experiment.

I would like to express my gratitude to all my friends in Lüdenscheid and Dortmund, some of them I know really well for many years, some even for decades. I hope we will stay in contact.

And finally, I am very grateful for the support my family gave to me. Especially my parents have given support to me all of my life, in every respect. Thanks to you!

Erklärung

Hiermit versichere ich, dass ich diese Arbeit selbstständig verfasst habe und keine anderen als die angegebenen Quellen und Hilfsmittel benutzt habe.

Thomas Bäcker